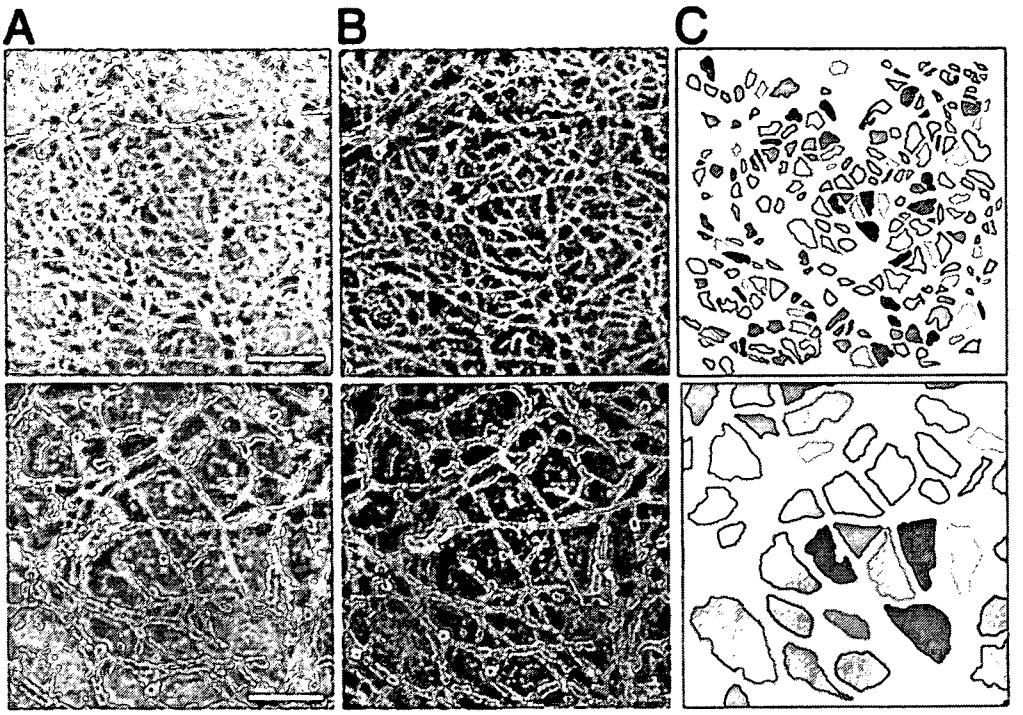

Figure 7. **The MSK meshwork directly on the cytoplasmic surface of the plasma membrane.** The central parts of the figures in the top row (bar, 300 nm) are magnified by a factor of three and are shown in the bottom row (bar, 100 nm). (A) Typical stereo views of the plasma membrane specimen (anaglyph; left = red). (B) Normal electron micrographs of the plasma membrane samples. The same view fields as those in A. (C) The areas delimited by the actin filaments closely apposed to the cytoplasmic surface of the cell membrane are shown. Different colors are shown to help the eye.

These results indicate that in the same cell line (for both the NRK and FRSK cases), the MSK mesh size determined by electron tomography and the diffusion compartment size determined by the high speed single-particle tracking of a phospholipid are similar to each other. However, between these two cell lines, both the MSK mesh and the diffusion compartment sizes differ greatly. The similarities between the MSK mesh sizes and the diffusion compartment sizes in cell lines that exhibit quite different distributions strongly support the MSK fence and picket models.

Discussion

We performed quantitative analyses of the undercoat structure of the cytoplasmic surface of the plasma membrane using electron tomography for samples prepared by a rapid-freeze, deep-etch, platinum replication technique. One of the most important limitations of this technique is that the cell has to be placed in a hypotonic medium at 4°C for 5–15 min to remove the upper cell membrane. However, with this method, large membrane fragments that were covered by the dense MSK meshwork could be obtained, which was important for the purpose of the present research.

We obtained the results by specifically addressing the following three questions. (1) Does the dense meshwork of the MSK exist everywhere on the cytoplasmic surface of the cell membrane, and, if so, how is it linked to the bulk cytoskeleton? (2) If so, what is its relationship with other structures of the plasma membrane, such as CCPs and caveolae? (3) How is the distribution of the MSK mesh size right on the cytoplasmic surface of the plasma membrane?

The final point is important because this part of the MSK might form the corrals of the plasma membrane for the diffusion of membrane molecules. Therefore, it is interesting to compare the distribution of the mesh size of the MSK directly attached to the cytoplasmic surface of the plasma membrane, as determined by an EM method, with that of the compartment size for the diffusion of membrane molecules. NRK (median size = 230 nm) and FRSK (41 nm) cell lines were selected for such a comparison because their compartment sizes are very different (Fujiwara et al., 2002; Murase et al., 2004). This will be an interesting test for the MSK fence and MSK-anchored transmembrane protein picket models and became possible by obtaining the 3D reconstructed images of the MSK structure on the cytoplasmic surface of the plasma membrane.

Does the dense meshwork of the MSK exist everywhere on the cytoplasmic surface of the cell membrane, and, if so, how is it linked to the bulk cytoskeleton?

The cytoplasmic surface of the plasma membrane has been observed by EM for >30 yr (Byers and Porter, 1977). Stunning high resolution EM images of the structures near the cytoplasmic surface have been published previously (Heuser and Kirschner,

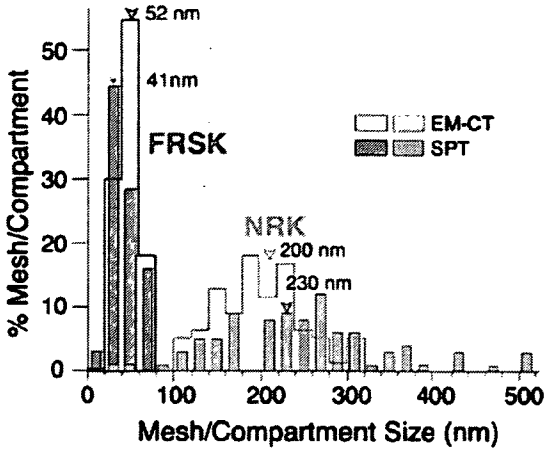

Figure 8. **Comparison of the distributions of the MSK mesh size on the cytoplasmic surface of the plasma membrane estimated by electron tomography with that of the compartment size determined from the phospholipid diffusion data for NRK and FRSK cells.** Electron tomography, open bars; phospholipid diffusion data, closed bars (adapted from Fujiwara et al., 2002 and Murase et al., 2004). NRK, pink; FRSK, blue. Within the same cell type, the MSK mesh size and diffusion compartment size exhibited similar distributions (compare the open and closed bars with the same color). The actual sizes are quite different between NRK and FRSK cells. EM-CT, EM-based computer tomograph; SPT, single-particle tracking.

1980; Hirokawa and Heuser, 1981; Heuser and Anderson, 1989; Hartwig and DeSisto, 1991; Rothberg et al., 1992), suggesting that the plasma membranes of animal cells are shaped by cytoskeletal interactions. However, despite these interesting and important studies, we felt that more extensive studies addressing the questions posed in the title of this subsection are necessary in particular for cells in culture.

We found that almost the entire cytoplasmic surface of the upper cell membrane is covered with the actin-based MSK except for the places where CCPs, caveolae, and noncoated membrane invaginations exist. In addition, this extensive pseudo-2D–type MSK network is linked to many actin filaments that extend from the membrane cytoplasmic surface toward the cytoplasm (Fig. 4 A) and is probably connected to the bulk cytoskeleton. This is consistent with the quantitative analysis of bleb formation, in which the density of the MSK filaments must be higher than one every 0.5–1 μm to avoid blebbing (Sheetz et al., 2006).

How closely is the MSK associated with CCPs and caveolae?

Almost all of the CCPs and caveolae are extensively linked to the MSK meshwork. As found in Figs. 2–4, many actin filaments that come out of the MSK meshwork are connected to these structures at their polygonal and striated patterns, respectively, and, in the cell types examined here, this occurs much more extensively than found previously (Rothberg et al., 1992; Fujimoto et al., 2000; Parton, 2003). Merrifield et al. (2002) found that actin rapidly becomes more concentrated at the CCPs right before they are internalized, but from the structures found in the present research, we could not tell what kind of actin–CCP interactions may be involved in such concentrations.

Is the distribution of the MSK mesh size right on the cytoplasmic surface of the plasma membrane consistent with that for the compartment size determined by a phospholipid diffusion probe?

3D reconstruction of the MSK using electron tomography allowed the determination of the MSK meshwork directly situated on the cytoplasmic surface of the plasma membrane. This meshwork is likely to partition the plasma membrane into many small compartments with regard to the lateral diffusion of membrane molecules. The size distribution of the areas bounded by the MSK meshwork agreed well with that determined for an unsaturated phospholipid undergoing hop diffusion in high speed single-particle tracking experiments in both NRK and FRSK cells, which have quite different mesh sizes (Fig. 8). These results support the MSK fence (corralling) model and the anchored transmembrane protein picket model.

How the MSK is attached to the cytoplasmic surface of the plasma membrane is unknown. Specific proteins that link the membrane and actin filaments at their barbed ends, such as gelsolin and villin (Pollard and Cooper, 1986; Hartwig et al., 1989), and at their sides, such as ponticulin (Wuestehube and Luna, 1987) and ezrin/radixin/moesin family proteins (Tsukita et al., 1997), exist. However, the weak nonspecific binding of actin filaments to membrane lipids and proteins may greatly contribute to the interactions of the actin filaments with the membrane. Although transmembrane proteins are temporarily trapped within a compartment, they hop to adjacent compartments in longer terms, suggesting that the link between the membrane and actin filaments may break at a rate comparable with the hop rate, which is once every several to several hundred milliseconds (depending on the molecule and cell type).

In addition to actin and actin-associated proteins, some other proteins may contribute to forming the MSK and membrane corrals. For example, septin, which is ~7-nm thick in the negatively stained images (Kinoshita et al., 2002), and agorin (Apgar and Mescher, 1986) may play some roles. Further characterization of the proteins involved in the MSK and its interaction with the membrane components and further analysis of the dynamics of membrane–MSK interactions will be important for understanding the roles played by the MSK–plasma membrane interactions in signal transduction, domain formation in the plasma membrane, and reorganization of the cytoskeleton.

Materials and methods

Antibodies and other reagents

Rabbit anti-actin IgG was obtained from Biomedical Technologies, and colloidal gold probes (5-nm diameter) coated with secondary antibodies (produced in goat) were purchased from GE Healthcare.

Rapid-freeze, deep-etch, immunoreplica EM of the cytoplasmic cell surface

NRK and FRSK cells were maintained in HAM-F12 or DME mediums, respectively, supplemented with 10% FBS (Sigma-Aldrich) under a 5% CO_2 atmosphere at 37°C. The cells used for the experiments were grown in 35-mm plastic dishes to ~70% confluency, usually 2 d after inoculation. The cells were washed three times with ice-cold Pipes buffer (10 mM Pipes, 100 mM KCl, 5 mM $MgCl_2$, and 3 mM EGTA, pH 6.8, which mimics the environment in the cytoplasm somewhat but is slightly hypotonic) and were exposed for 15–30 s to an ice-cold 70% Pipes buffer (the Pipes buffer diluted by a factor of 1.43 with water, making this solution more hypotonic;

Rutter et al., 1988). After the buffer on the coverslip was drained, the remaining excess water was removed by filter paper. To expose the cytoplasmic surface of the upper cell membrane, the upper cell membrane was removed from the rest of the cell after it was adhered to a coverslip placed on top of the cell layer (Rutter et al., 1988; Sanan and Anderson, 1991). 5 × 5-mm coverslips (Matsunami) coated with positively charged Alcian blue 8GX (Wako; Alcian blue–coated coverslips were prepared by first immersing them in 1% Alcian blue in distilled water at room temperature for 10 min, washing them with distilled water, and drying them in the air) were placed on top of the cells (upper surface facing the medium rather than the coverslip) and incubated at 4°C for 5–15 min. During this period, good contact between the cell surface and the coverslip was developed. Then, the coverslips were gently floated off from the cell using the surface tension of the buffer by slowly adding ice-cold Pipes buffer containing 1% PFA/0.25% glutaraldehyde into the space between the culture dish and the coverslip. When the coverslip floated off, the cells were cleaved, and the upper cell membrane came off with the coverslip. Then, the cells were further fixed by incubation in fresh ice-cold 1% PFA/0.25% glutaraldehyde in Pipes buffer for 10 min. After fixation, the coverslips were washed three times, for 10 min each time, with PBS (8.10 mM Na_2HPO_4, 1.47 mM KH_2PO_4, 137 mM NaCl, and 2.68 mM KCl, pH 7.4).

To identify the actin filaments on the cytoplasmic surface of the cell membrane, immunogold labeling was performed after fixation. The fixed upper cell membranes on the coverslips with their cytoplasmic surfaces exposed toward the buffer were incubated at 4°C for 2 h in PBS containing 10 μg/ml rabbit anti-actin IgG and 1% BSA (Sigma-Aldrich), and, after three washes for 10 min each in 25 mM Tris-buffer, pH 8.0, the cell membranes were incubated in Tris-buffer containing 1% BSA and 5-nm–diameter colloidal gold conjugated with anti–rabbit IgG goat antibodies (GE Healthcare) at 4°C for 2 h. After three washes in PBS, these labeled membranes were further fixed in 2% glutaraldehyde in PBS on ice for 5 min. Finally, the coverslips were washed in distilled water for 1 min before rapid freezing.

Each coverslip was placed on the plunger tip of the rapid-freezing device (Eiko; Usukura and Yamada, 1987) with the cytoplasmic surface of the membrane facing down. The specimen was slammed down (free fall) onto a polished pure copper block, which was precooled by direct immersion in liquid helium. The frozen coverslip was placed in liquid nitrogen and was transferred into the freeze-etching shadowing chamber (FR7000-S; Hitachi). The excess ice covering the cytoplasmic surface of the membrane was shaved off with a prechilled glass knife using a microtome placed in the chamber at −140°C or below. The cytoplasmic surface was then etched for ~10 min after the specimen temperature was raised to −90°C. The etched specimen surfaces were then rotary shadowed with platinum at an angle of 22.5° from the surface and with carbon from the top. The molecules as well as the gold probes localized on the cytoplasmic surface of the cell membrane were immobilized to the deposited platinum (Fujimoto, 1995; Fujimoto et al., 1996).

Collodion was applied immediately after the platinum-carbon replicas were removed from the cold chamber to fortify them. The platinum-carbon replica was removed from the glass coverslip in 1% hydrofluoric acid in distilled water. After the replicas were successfully removed from the glass surface and mounted on the grid, the collodion coat was dissolved away in n-pentyl acetate. In this protocol, the sodium hypochlorite solution, which is generally used to remove the replicas from the coverslip and also to clear the membrane and the undercoat structure of the replicas, was replaced with 1% hydrofluoric acid to keep the cell membrane, the undercoat structure, and the immunogold probes that had been attached to these structures on the platinum replicas (1% hydrofluoric acid is likely to only dissolve the glass, leaving the cell membrane molecules bound to the platinum replica; Fujimoto, 1995; Fujimoto et al., 1996). An additional advantage of using 1% hydrofluoric acid is that the platinum replicas break less often, probably because it does not remove the membrane components and, thus, leaves the replicas rather intact. In addition, to keep as many colloidal gold particles and membrane molecules attached to the platinum replicas as possible, we included Photo-Flo 200 (Kodak), a detergent used to prevent water-drop stains on photographic film in all of the solutions used here (advice given by J. Heuser). After the replicas were washed with distilled water, they were mounted on 100–200 mesh copper grids (Ted Pella) coated with polyvinyl formvar (Nisshin EM) and observed at magnifications of ~10,000–70,000 with a transmission electron microscope (1200EX; JEOL).

The following methodological precautions and improvements were made to reproducibly produce large cell membranes and replicas without excessive fragmentation. (1) An Alcian blue coat rather than poly-L-lysine coat was used (Rutter et al., 1988; Sanan and Anderson, 1991). (2) Before overlaying the coverslips, excess water was removed from the specimen, leaving just enough buffer to cover the cell. (3) To cleave off the upper membrane attached to the overlaid coverslip, the coverslip was floated off very gently by adding cleavage medium (using the surface tension of the buffer to float the coverslip). If this was not performed gently enough, the membrane was fragmented. (4) The frozen sample was shaved with a glass knife, with the angle between the knife and the coverglass adjusted to a shallow angle (<6°) so that most of the excess water and the cytoplasm were removed and the cytoplasmic surface of the cell membrane could be exposed after light etching. Because replicas with too many variations in height tend to break when they are removed from the coverslip and placed on the water surface, removal of the excess cytoplasm helps to avoid replica breakage. (5) Collodion was applied immediately after the replicas were removed from the cold chamber (before the replicas were removed from the coverslip on the water surface) to fortify the replica (a technique learned from T. Baba and S. Ohno). This step also helped to prevent replica breakage when the replicas were removed from the coverslip. After the large replicas were removed from the glass surface, the collodion coat was dissolved away in n-pentyl acetate. (6) A solution of 1% hydrofluoric acid was used to slightly dissolve the glass surface to facilitate the removal of replicas from the coverslip. (7) A detergent, Photo-Flo 200 (Kodak), was included in all of the solutions that contacted platinum replicas.

Electron microscope tomography

For 3D reconstruction, the replica was imaged at tilt angles of every 1.0° in the range between ±48 and 70° (total of 97–141 images) for a single field by a transmission electron microscope (Tecnai Sphera F20; FEI) equipped with a CCD camera (1,024 × 1,024 pixels). The pixel size at the specimen was 0.85 nm. The image acquisition was fully automated as previously described (Medalia et al., 2002). The 100–121 image sections of every 0.85–1.34 nm were obtained by a calculation based on the set of 97–141 tilt images using an IMOD software package running on Linux (University of Colorado; Kremer et al., 1996). Corrections for the tilt of the specimen and the long wavelength undulations of the membrane were also achieved with IMOD software. 3D rendering (displaying 3D images in different ways) was performed using the Amira DEV software package (Mercury Computer Systems) operating on a Linux system.

Analysis of the 3D reconstructed images of the MSK

In the series of electron tomography sections shown in Fig. 6 (A and B), the existence of three major classes of filaments with regard to the distance from the membrane surface was found in the following way. The first class is the filaments that are highly electron dense in the first ~0–1.7-nm section (because the contrast is reversed in these micrographs, they look more lucent or white) and are continuously seen in the image sections up to the ~6.8–8.5-nm section, which then dim rapidly in the ~8.5–10.2- and ~10.2–11.9-nm sections. To quantitatively evaluate such signal intensity changes within individual filaments, we selected points that are clearly seen in the image of the first ~0–1.7-nm section every 100–250 nm on each filament, measured the signal intensity on each spot (five pixels), and looked for the section where the signal intensity on the spot decreases by >25% from that for the adjacent section closer to the membrane (the signal intensity tends to drop very rapidly around the threshold sections). If the 25% decrease in the signal intensity occurred between the sections of ~6.8–8.5 and ~8.5–10.2 nm or between the sections of ~8.5–10.2 and ~10.2–11.9 nm, these filaments were categorized into the first class (i.e., those closely associated with the cytoplasmic surface of the cell membrane). These filaments are drawn in green in Fig. 6 C (different regions within a single filament might become dim in either of these two sections).

The second class is similar to the first class but can be seen clearly even in the ~10.2–11.9-nm section (and also in the ~11.9–13.6-nm section, which usually looked similar to the ~10.2–11.9-nm section). This may be the result of the actin filaments that are located several nanometers away from the cytoplasmic surface. Because the platinum rotary shadowing was performed at a low angle (22° from the surface), the platinum may have been deposited in the space between the filament and the membrane. Another possibility is that two filaments are stacked together for a long distance, but we do not think that this happens very often. Therefore, we categorized these filaments into those that stay near the membrane but do not closely associate with the membrane surface. These filaments were not considered to contribute to delimiting the membrane compartments for molecular diffusion in the plasma membrane.

The third class is the filaments that exhibit dim signals in the first ~0–1.7-nm section and show higher electron densities in farther sections, at least up to the section of ~10.2–11.9 nm, before fading out in the ~11.9–13.6- and ~13.6–15.3-nm sections (the latter two sections are not depicted).

These filaments were again assumed not to contribute to forming membrane corrals. The second and third classes of filaments are drawn in red in Fig. 6 C.

There were regions that were not amenable to such analysis. They were the areas where bundles of actin filaments were present (e.g., the structure crossing diagonally from the bottom left to the top right in Fig. 5), actin filaments were too crowded to be individually discerned, an actin filament was terminated in the middle of a domain (domains that contain a loose end of an actin filament), or CCPs, caveolae, and the smooth surface membrane invaginations were present. They were excluded from this analysis (Fig. 7 C, white regions).

Online supplemental material

Video 1 shows a series of 131 tilt images of the undercoat structure on the cytoplasmic surface. Video 2 presents a 3D reconstructed image of the undercoat structure on the cytoplasmic surface of the plasma membrane, which is shown by rotating the reconstructed image. Video 3 shows a series of 97 tilt images of the MSK in an NRK cell, and Video 4 shows a series of 121 sliced images of every 0.85 nm of the MSK of an NRK cell calculated from the data shown in Video 3. Online supplemental material is available at http://www.jcb.org/cgi/content/full/jcb.200606007/DC1.

We thank Y. Hirata (FEI) for her help in starting us with electron tomography, Drs. T. Baba and S. Ohno (Yamanashi University Medical School) for their help in preparing large platinum replicas, Dr. Mitsutoshi Setou (Mitsubishi Kagaku Institute of Life Sciences) for encouragement, and Dr. J. Heuser (Washington University) for helpful discussions and encouragement.

This research was supported, in part, by a Health Labor Sciences Research grant (nano-001 to N. Morone), a National Institute of Biomedical Innovation grant (05-32 to S. Yuasa), and Grants-in-Aid for Scientific Research and on Priority Areas from the Ministry of Education, Culture, Sports, Science and Technology (to J. Usukura and A. Kusumi).

Submitted: 2 June 2006
Accepted: 4 August 2006

References

Apgar, J.R., and M.F. Mescher. 1986. Agorins: major structural proteins of the plasma membrane skeleton of P815 tumor cells. *J. Cell Biol.* 103:351–360.

Bennett, V. 1990. Spectrin-based membrane skeleton: a multipotential adaptor between plasma membrane and cytoplasm. *Physiol. Rev.* 70:1029–1065.

Bennett, V., and L. Chen. 2001. Ankyrins and cellular targeting of divers membrane proteins to physiological sites. *Curr. Opin. Cell Biol.* 13:61–67.

Branton, D., C.M. Cohen, and J. Tyler. 1981. Interaction of cytoskeletal proteins on the human erythrocyte membrane. *Cell.* 24:24–32.

Bussell, S.J., D.A. Hammer, and D.L. Koch. 1994. The effect of hydrodynamic interactions on the tracer and gradient diffusion of integral membrane-proteins in lipid bilayers. *J. Fluid Mech.* 258:167–190.

Bussell, S.J., D.L. Koch, and D.A. Hammer. 1995. Effect of hydrodynamic interactions on the diffusion of integral membrane proteins: diffusion in plasma membranes. *Biophys. J.* 68:1836–1849.

Byers, H.R., and K.R. Porter. 1977. Transformations in the structure of the cytoplasmic ground substance in erythrophores during pigment aggregation and dispersion. I. A study using whole-cell preparations in stereo high voltage electron microscopy. *J. Cell Biol.* 75:541–558.

Discher, D.E., R. Winardi, P.O. Schischmanoff, M. Parra, J.G. Conboy, and N. Mohandas. 1995. Mechanochemistry of protein 4.1's spectrin-actin-binding domain: ternary complex interactions, membrane binding, network integration, structural strengthening. *J. Cell Biol.* 130:897–907.

Edidin, M., S.C. Kuo, and M.P. Sheetz. 1991. Lateral movements of membrane glycoproteins restricted by dynamic cytoplasmic barriers. *Science.* 254:1379–1382.

Fujimoto, K. 1995. Freeze-fracture replica electron microscopy combined with SDS digestion for cytochemical labeling of integral membrane proteins. Application to the immunogold labeling of intercellular junctional complexes. *J. Cell Sci.* 108:3443–3449.

Fujimoto, K., M. Umeda, and T. Fujimoto. 1996. Transmembrane phospholipid distribution revealed by freeze-fracture replica labeling. *J. Cell Sci.* 109:2453–2460.

Fujimoto, L.M., R. Roth, J.E. Heuser, and S.L. Schmid. 2000. Actin assembly plays a variable, but not obligatory role in receptor-mediated endocytosis in mammalian cells. *Traffic.* 1:161–171.

Fujiwara, T., K. Ritchie, H. Murakoshi, K. Jacobson, and A. Kusumi. 2002. Phospholipids undergo hop diffusion in compartmentalized cell membrane. *J. Cell Biol.* 157:1071–1081.

Gaidarov, I., F. Santini, R.A. Warren, and J.H. Keen. 1999. Spatial control of coated-pit dynamics in living cells. *Nat. Cell Biol.* 1:1–7.

Hartwig, J.H., and H.L. Yin. 1988. The organization and regulation of the macrophage actin skeleton. *Cell Motil. Cytoskeleton.* 10:117–125.

Hartwig, J.H., and M. DeSisto. 1991. The cytoskeleton of the resting human blood platelet: structure of the membrane skeleton and its attachment to actin filaments. *J. Cell Biol.* 112:407–425.

Hartwig, J.H., K.A. Chambers, and T.P. Stossel. 1989. Association of gelsolin with actin filaments and cell membranes of macrophages and platelets. *J. Cell Biol.* 108:467–479.

Heuser, J.E. 1983. Procedure for freeze-drying molecules adsorbed to mica flakes. *J. Mol. Biol.* 169:155–195.

Heuser, J.E., and M.W. Kirschner. 1980. Filament organization revealed in platinum replicas of freeze-dried cytoskeletons. *J. Cell Biol.* 86:212–234.

Heuser, J.E., and R.G. Anderson. 1989. Hypertonic media inhibit receptor-mediated endocytosis by blocking clathrin-coated pit formation. *J. Cell Biol.* 108:389–400.

Hirokawa, N., and J.E. Heuser. 1981. Quick-freeze, deep-etch visualization of the cytoskeleton beneath surface differentiations of intestinal epithelial cells. *J. Cell Biol.* 91:399–409.

Iino, R., I. Koyama, and A. Kusumi. 2001. Single molecule imaging of green fluorescent proteins in living cells: E-cadherin forms oligomers on the free cell surface. *Biophys. J.* 80:2667–2677.

Jacobson, K., E.D. Sheets, and R. Simson. 1995. Revisiting the fluid mosaic model of membranes. *Science.* 268:1441–1442.

Katayama, E. 1998. Quick-freeze deep-etch electron microscopy of the actin-heavy meromyosin complex during the in vitro motility assay. *J. Mol. Biol.* 278:349–367.

Kinoshita, M., C.M. Field, M.L. Coughlin, A.F. Straight, and T.J. Mitchison. 2002. Self- and actin-templated assembly of Mammalian septins. *Dev. Cell.* 3:791–802.

Kremer, J.R., D.N. Mastronarde, and J.R. McIntosh. 1996. Computer visualization of three-dimensional image data using IMOD. *J. Struct. Biol.* 116:71–76.

Kusumi, A., and Y. Sako. 1996. Cell surface organization by the membrane skeleton. *Curr. Opin. Cell Biol.* 8:566–574.

Kusumi, A., C. Nakada, K. Ritchie, K. Murase, K. Suzuki, H. Murakoshi, R.S. Kasai, J. Kondo, and T. Fujiwara. 2005. Paradigm shift of the plasma membrane concept from the two-dimensional continuum fluid to the partitioned fluid: high-speed single-molecule tracking of membrane molecules. *Annu. Rev. Biophys. Biomol. Struct.* 34:351–378.

Lucic, V., F. Forster, and W. Baumeister. 2005. Structural studies by electron tomography: from cells to molecules. *Annu. Rev. Biochem.* 74:833–865.

Luna, E.J., and A.L. Hitt. 1992. Cytoskeleton–plasma membrane interactions. *Science.* 258:955–964.

McIntosh, R., D. Nicastro, and D. Mastronarde. 2005. New views of cells in 3D: an introduction to electron tomography. *Trends Cell Biol.* 15:43–51.

Medalia, O., I. Weber, A.S. Frangakis, D. Nicastro, G. Gerisch, and W. Baumeister. 2002. Macromolecular architecture in eukaryotic cells visualized by cryoelectron tomography. *Science.* 298:1209–1213.

Merrifield, C.J., M.E. Feldman, L. Wan, and W. Almers. 2002. Imaging actin and dynamin recruitment during invagination of single clathrin-coated pits. *Nat. Cell Biol.* 4:691–698.

Mohandas, N., and E. Evans. 1994. Mechanical properties of the red cell membrane in relation to molecular structure and genetic defects. *Annu. Rev. Biophys. Biomol. Struct.* 23:787–818.

Moritz, M., M.B. Braunfeld, V. Guenebaut, J. Heuser, and D.A. Agard. 2000. Structure of the gamma-tubulin ring complex: a template for microtubule nucleation. *Nat. Cell Biol.* 2:365–370.

Murase, K., T. Fujiwara, Y. Umemura, K. Suzuki, R. Iino, H. Yamashita, M. Saito, H. Murakoshi, K. Ritchie, and A. Kusumi. 2004. Ultrafine membrane compartments for molecular diffusion as revealed by single molecule techniques. *Biophys. J.* 86:4075–4093.

Pan, Z., T. Kao, Z. Horvath, J. Lemos, J.Y. Sul, S.D. Cranstoun, V. Bennett, S.S. Scherer, and E.C. Cooper. 2006. A common ankyrin-G-based mechanism retains KCNQ and NaV channels at electrically active domains of the axon. *J. Neurosci.* 26:599–613.

Parton, R.G. 2003. Caveolae–from ultrastructure to molecular mechanisms. *Nat. Rev. Mol. Cell Biol.* 4:162–167.

Perkins, G.A., C.W. Renken, J.Y. Song, T.G. Frey, S.J. Young, S. Lamont, M.E. Martone, S. Lindsey, and M.H. Ellisman. 1997. Electron tomography of large, multicomponent biological structures. *J. Struct. Biol.* 120:219–227.

Pollard, T.D., and J.A. Cooper. 1986. Actin and actin-binding proteins. A critical evaluation of mechanisms and functions. *Annu. Rev. Biochem.* 55:987–1035.

Qualmann, B., M.M. Kessels, and R.B. Kelly. 2000. Molecular links between endocytosis and the actin cytoskeleton. *J. Cell Biol.* 150:F111–F116.

Rothberg, K.G., J.E. Heuser, W.C. Donzell, Y.S. Ying, J.R. Glenney, and R.G. Anderson. 1992. Caveolin, a protein component of caveolae membrane coats. *Cell.* 68:673–682.

Rutter, G., W. Bohn, H. Hohenberg, and K. Mannweiler. 1988. Demonstration of antigens at both sides of plasma membranes in one coincident electron microscopic image: a double-immunogold replica study of virus-infected cells. *J. Histochem. Cytochem.* 36:1015–1021.

Sako, Y., and A. Kusumi. 1994. Compartmentalized structure of the plasma membrane for receptor movements as revealed by a nanometer-level motion analysis. *J. Cell Biol.* 125:1251–1264.

Sako, Y., and A. Kusumi. 1995. Barriers for lateral diffusion of transferrin receptor in the plasma membrane as characterized by receptor dragging by laser tweezers: fence versus tether. *J. Cell Biol.* 129:1559–1574.

Sako, Y., A. Nagafuchi, S. Tsukita, M. Takeichi, and A. Kusumi. 1998. Cytoplasmic regulation of the movement of E-cadherin on the free cell surface as studied by optical tweezers and single particle tracking: corralling and tethering by the membrane skeleton. *J. Cell Biol.* 140:1227–1240.

Sanan, D.A., and R.G. Anderson. 1991. Simultaneous visualization of LDL receptor distribution and clathrin lattices on membranes torn from the upper surface of cultured cells. *J. Histochem. Cytochem.* 39:1017–1024.

Saxton, M.J. 1989. The spectrin network as a barrier to lateral diffusion in erythrocytes. A percolation analysis. *Biophys. J.* 55:21–28.

Saxton, M.J. 1990. The membrane skeleton of erythrocytes. A percolation model. *Biophys. J.* 57:1167–1177.

Saxton, M.J., and K. Jacobson. 1997. Single-particle tracking: applications to membrane dynamics. *Annu. Rev. Biophys. Biomol. Struct.* 26:373–399.

Schoenenberger, C.A., M.O. Steinmetz, D. Stoffler, A. Mandinova, and U. Aebi. 1999. Structure, assembly, and dynamics of actin filaments in situ and in vitro. *Microsc. Res. Tech.* 47:38–50.

Sheetz, M.P. 1983. Membrane skeletal dynamics: role in modulation of red cell deformability, mobility of transmembrane proteins, and shape. *Semin. Hematol.* 20:175–188.

Sheetz, M.P., and D. Sawyer. 1978. Triton shells of intact erythrocytes. *J. Supramol. Struct.* 8:399–412.

Sheetz, M.P., J.E. Sable, and H.G. Dobereiner. 2006. Continuous membrane-cytoskeleton adhesion requires continuous accommodation to lipid and cytoskeleton dynamics. *Annu. Rev. Biophys. Biomol. Struct.* 35:417–434.

Shen, B.W., R. Josephs, and T.L. Steck. 1986. Ultrastructure of the intact skeleton of the human erythrocyte membrane. *J. Cell Biol.* 102:997–1006.

Suzuki, K., K. Ritchie, E. Kajikawa, T. Fujiwara, and A. Kusumi. 2005. Rapid hop diffusion of a G-protein-coupled receptor in the plasma membrane as revealed by single-molecule techniques. *Biophys. J.* 88:3659–3680.

Takeuchi, M., H. Miyamoto, Y. Sako, H. Komizu, and A. Kusumi. 1998. Structure of the erythrocyte membrane skeleton as observed by atomic force microscopy. *Biophys. J.* 74:2171–2183.

Tomishige, M., Y. Sako, and A. Kusumi. 1998. Regulation mechanism of the lateral diffusion of band 3 in erythrocyte membranes by the membrane skeleton. *J. Cell Biol.* 142:989–1000.

Tsuji, A., and S. Ohnishi. 1986. Restriction of the lateral motion of band 3 in the erythrocyte membrane by the cytoskeletal network: dependence on spectrin association state. *Biochemistry.* 25:6133–6139.

Tsuji, A., K. Kawasaki, S. Ohnishi, H. Merkle, and A. Kusumi. 1988. Regulation of band 3 mobilities in erythrocyte ghost membranes by protein association and cytoskeletal meshwork. *Biochemistry.* 27:7447–7452.

Tsukita, S., S. Tsukita, and H. Ishikawa. 1980. Cytoskeletal network underlying the human erythrocyte membrane. Thin-section electron microscopy. *J. Cell Biol.* 85:567–576.

Tsukita, S., S. Yonemura, and S. Tsukita. 1997. ERM proteins: head-to-tail regulation of actin-plasma membrane interaction. *Trends Biochem. Sci.* 22:53–58.

Ursitti, J.A., D.W. Pumplin, J.B. Wade, and R.J. Bloch. 1991. Ultrastructure of the human erythrocyte cytoskeleton and its attachment to the membrane. *Cell Motil. Cytoskeleton.* 19:227–243.

Usukura, J., and E. Yamada. 1987. Ultrastructure of the synaptic ribbons in photoreceptor cells of *Rana catesbeiana* revealed by freeze-etching and freeze-substitution. *Cell Tissue Res.* 247:483–488.

Valentijn, J.A., K. Valentijn, L.M. Pastore, and J.D. Jamieson. 2000. Actin coating of secretory granules during regulated exocytosis correlates with the release of rab3D. *Proc. Natl. Acad. Sci. USA.* 97:1091–1095.

Wuestehube, L.J., and E.J. Luna. 1987. F-actin binds to the cytoplasmic surface of ponticulin, a 17-kD integral glycoprotein from *Dictyostelium discoideum* plasma membranes. *J. Cell Biol.* 105:1741–1751.

Zeuschner, D., W.J. Geerts, E. van Donselaar, B.M. Humbel, J.W. Slot, A.J. Koster, and J. Klumperman. 2006. Immuno-electron tomography of ER exit sites reveals the existence of free COPII-coated transport carriers. *Nat. Cell Biol.* 8:377–383.

Ubiquitin C-terminal hydrolase L1 regulates the morphology of neural progenitor cells and modulates their differentiation

Mikako Sakurai[1,2], Koichi Ayukawa[1], Rieko Setsuie[1,2], Kaori Nishikawa[1], Yoko Hara[1], Hiroki Ohashi[1,3], Mika Nishimoto[1,4], Toshiaki Abe[3], Yoshihisa Kudo[4], Masayuki Sekiguchi[1], Yae Sato[1,2], Shunsuke Aoki[1], Mami Noda[2] and Keiji Wada[1,*]

[1]Department of Degenerative Neurological Diseases, National Institute of Neuroscience, National Center of Neurology and Psychiatry, Kodaira, Tokyo, 187-8502, Japan
[2]Laboratory of Pathophysiology, Graduate School of Pharmaceutical Sciences, Kyushu University, Higashi-ku, Fukuoka, 812-8582, Japan
[3]Department of Neurosurgery, Graduate School of Medicine, Jikei University School of Medicine, Minato-ku, Tokyo, 105-8461, Japan
[4]Laboratory of Cellular Neurobiology, Tokyo University of Pharmacy and Life Science, Hachioji, Tokyo, 192-0392, Japan
*Author for correspondence (e-mail: wada@ncnp.go.jp)

Accepted 27 September 2005
Journal of Cell Science 119, 162-171 Published by The Company of Biologists 2006
doi:10.1242/jcs.02716

Summary

Ubiquitin C-terminal hydrolase L1 (UCH-L1) is a component of the ubiquitin system, which has a fundamental role in regulating various biological activities. However, the functional role of the ubiquitin system in neurogenesis is not known. Here we show that UCH-L1 regulates the morphology of neural progenitor cells (NPCs) and mediates neurogenesis. UCH-L1 was expressed in cultured NPCs as well as in embryonic brain. Its expression pattern in the ventricular zone (VZ) changed between embryonic day (E) 14 and E16, which corresponds to the transition from neurogenesis to gliogenesis. At E14, UCH-L1 was highly expressed in the ventricular zone, where neurogenesis actively occurs; whereas its expression was prominent in the cortical plate at E16. UCH-L1 was very weakly detected in the VZ at E16, which corresponds to the start of gliogenesis. In cultured proliferating NPCs, UCH-L1 was co-expressed with nestin, a marker of undifferentiated cells. In differentiating cells, UCH-L1 was highly co-expressed with the early neuronal marker TuJ1. Furthermore, when UCH-L1 was induced in nestin-positive progenitor cells, the number and length of cellular processes of the progenitors decreased, suggesting that the progenitor cells were differentiating. In addition, NPCs derived from *gad* (UCH-L1-deficient) mice had longer processes compared with controls. The ability of UCH-L1 to regulate the morphology of nestin-positive progenitors was dependent on its binding affinity for ubiquitin but not on hydrolase activity; this result was also confirmed using *gad*-mouse-derived NPCs. These results suggest that UCH-L1 spatially mediates and enhances neurogenesis in the embryonic brain by regulating progenitor cell morphology.

Key words: PGP9.5, UCH-L1, Nestin, Ubiquitin, Cell morphology, Differentiation, Progenitor

Introduction

Ubiquitin C-terminal hydrolase L1 (UCH-L1) is a member of the deubiquitylating enzymes and is one of the most abundant proteins in the brain. Whereas other UCH members are ubiquitously expressed, UCH-L1 is selectively expressed in neurons and testes/ovaries in the adult (Wilkinson et al., 1989). UCH-L1 is also known as PGP9.5 and is used as a neuron-specific marker in neuroanatomical and neuropathological studies (Dickson et al., 1994; McQuaid et al., 1995). Recent studies suggest that UCH-L1 is involved in neurodegeneration. The I93M mutation and the S18Y polymorphism in UCH-L1 are implicated in Parkinson's disease (Leroy et al., 1998; Satoh and Kuroda, 2001). Using gracile axonal dystrophy (*gad*) mice, we previously demonstrated that the dying-back type of axonal degeneration is caused by a deletion of the *Uchl1* gene (Saigoh et al., 1999). UCH-L1 has an affinity for ubiquitin and ensures its stability within neurons in vivo (Osaka et al., 2003). Furthermore, UCH-L1 has ubiquitin ligase activity (Liu et al., 2002). Thus, UCH-L1 might have multiple functions and more roles in biological phenomena than previously expected.

UCH-L1 mRNA is first detected at embryonic day (E) 8.5-9 in the neural tube and in the neural epithelium (Schofield et al., 1995). In addition, UCH-L1 immunoreactivity has been observed in the neural tube at E10.5 (Sekiguchi et al., 2003). However, its functional role in embryonic neurogenesis is not well understood. CDK5 and Dab1 are involved in regulating the migratory behavior of postmitotic neurons. Both p35, which is a CDK5 kinase, and Dab1 are degraded by the ubiquitin-proteasome pathway (Arnaud et al., 2003; Bock et al., 2004; Patrick et al., 1998). Thus, the ubiquitin system might be important in the migration and differentiation of postmitotic neurons and for the lamination pattern of the cerebral cortex.

Neural progenitor cells (NPCs) differentiate into neurons, astrocytes and oligodendrocytes (Qian et al., 1998; Qian et al., 2000; Shen et al., 1998). In the embryonic brain, neuroepithelial cells and radial glia are present in the ventricular zone (VZ); neurogenesis occurs first, followed by

gliogenesis. Committed progenitor cells move from the VZ to the cortical plate (CP) (Noctor et al., 2004). The differentiating cells migrate by means of radial migration, during which the migrating cells change their morphology (Kawauchi et al., 2003; Noctor et al., 2002; Tabata and Nakajima, 2003). Here, we analyzed the functional role of UCH-L1 using mouse embryonic NPCs. Our results indicate that UCH-L1 is expressed in nestin-positive NPCs and might regulate neurogenesis. The expression pattern of UCH-L1 changed in parallel with the transition from neuronal generation to glial generation. Furthermore, UCH-L1 modulated the length of nestin-positive processes in NPCs. Our results constitute the first evidence that UCH-L1 is important in neurogenesis and thus provide the basis for further investigation into the role of the ubiquitin system in neurogenesis.

Results

UCH-L1 expression in embryonic mouse brain

We first determined the specificity of the UCH-L1 antibody using immunoblotting (data not shown) and immunostaining. Because *gad* mice do not express endogenous UCH-L1 (Saigoh et al., 1999), we used these mice as a negative control. Heterozygous littermates had UCH-L1 immunostaining, whereas UCH-L1 immunoreactivity was not detected in the brains of *gad* mice (Fig. 1). These results confirmed the specificity of the antibody against UCH-L1. Using this antibody, we further compared the distribution and expression of UCH-L1 with the neural progenitor marker nestin and the early neuronal marker TuJ1. Nestin was expressed in the VZ of brains from both *gad* and heterozygous mice at E13 (Fig. 1). Nestin expression was observed throughout the region, whereas TuJ1 immunoreactivity was detected at the marginal zone (MZ). In heterozygous mice, UCH-L1 and nestin immunostaining overlapped in almost all cells in the VZ, suggesting that UCH-L1 is expressed in NPCs (Fig. 1A). TuJ1 expression colocalized with that of UCH-L1 in MZ cells, indicating that UCH-L1 is expressed in embryonic neurons as well (Fig. 1B). In E13 *gad* mouse brain, nestin staining differed compared with that in heterozygous littermates. Nestin staining was observed in many long radial fibers in the mutant, which we believed were radial glia; by contrast, staining in the heterozygotes occurred in radial glia as well as in neuronal cells at various stages of development (Fig. 1A; arrow and arrowhead).

We then looked for developmental changes in UCH-L1 expression. In the embryonic cerebral cortex, asymmetric cell division generates one neuron and one neural progenitor (Roegiers and Jan, 2004; Zhong et al., 1996; Zhong et al., 1997). These asymmetric cell divisions begin at E11, peak around E14, and subside after E16. At E14, astrocytes and oligodendrocytes are not yet present. However, at E16, glial cell production begins. The regional expression level for both nestin and TuJ1 did not change between E14 and E16 (Fig. 2A,B). At E14 and E16, nestin immunoreactivity was stronger in the VZ (Fig. 2A) and was faintly detected only along radial glial fibers in the CP (Fig. 2A,C; arrowhead) (Malatesta et al., 2003; Malatesta et al., 2000). TuJ1 immunoreactivity was predominantly detected in the MZ, CP, intermediate zone and subventricular zone at E14 and E16 (Fig. 2B,D). In the VZ, TuJ1 immunoreactivity was detected only in migrating neurons (Fig. 2D; arrowhead).

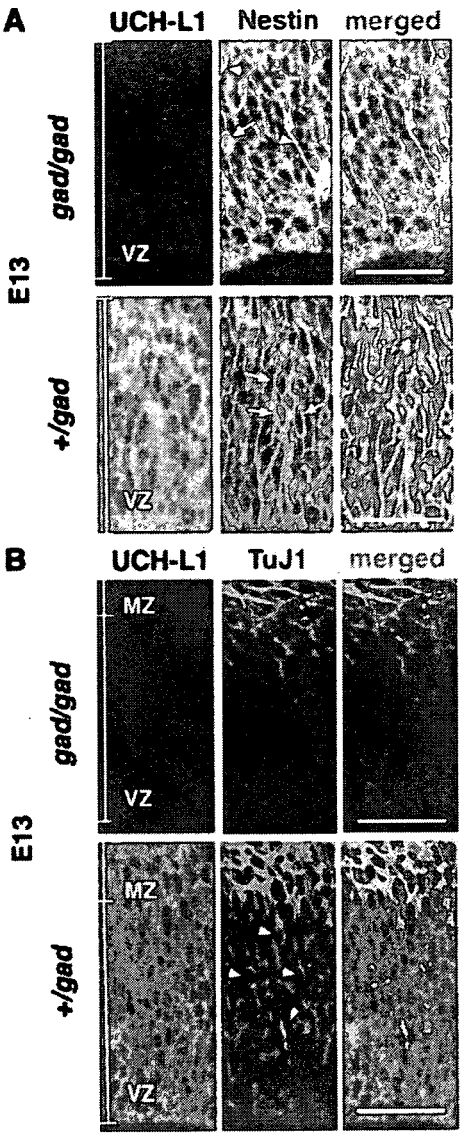

Fig. 1. Antibody specificity and expression of UCH-L1 in the ventricular zone at E13. UCH-L1 expression was detected using immunohistochemistry with anti-PGP9.5. UCH-L1 is not detected in the brain of *gad* mice at E13 (A,B) but is strongly expressed in heterozygous littermates (A,B). Confocal microscopic images of coronal sections of *gad* mice and heterozygous littermates were double stained with antibodies for the progenitor marker nestin and UCH-L1 (PGP9.5) (A) or for the early neuronal marker tubulin β III (TuJ1) and UCH-L1 (B). Long radial fibers are indicated by arrowheads, and various phases of progenitor cells are indicated by arrows (A). TuJ1-positive, migrating neuronal cells are indicated by arrowheads (B). MZ, marginal zone; VZ, ventricular zone. Bars, 40 μm.

By contrast, the pattern of UCH-L1 expression changed between E14 and E16 (Fig. 2A,B). At both stages of development, UCH-L1 was expressed in neuronal cells as well as in progenitor cells. UCH-L1 immunoreactivity was stronger in the VZ than in the CP at E14; however, the immunoreactivity

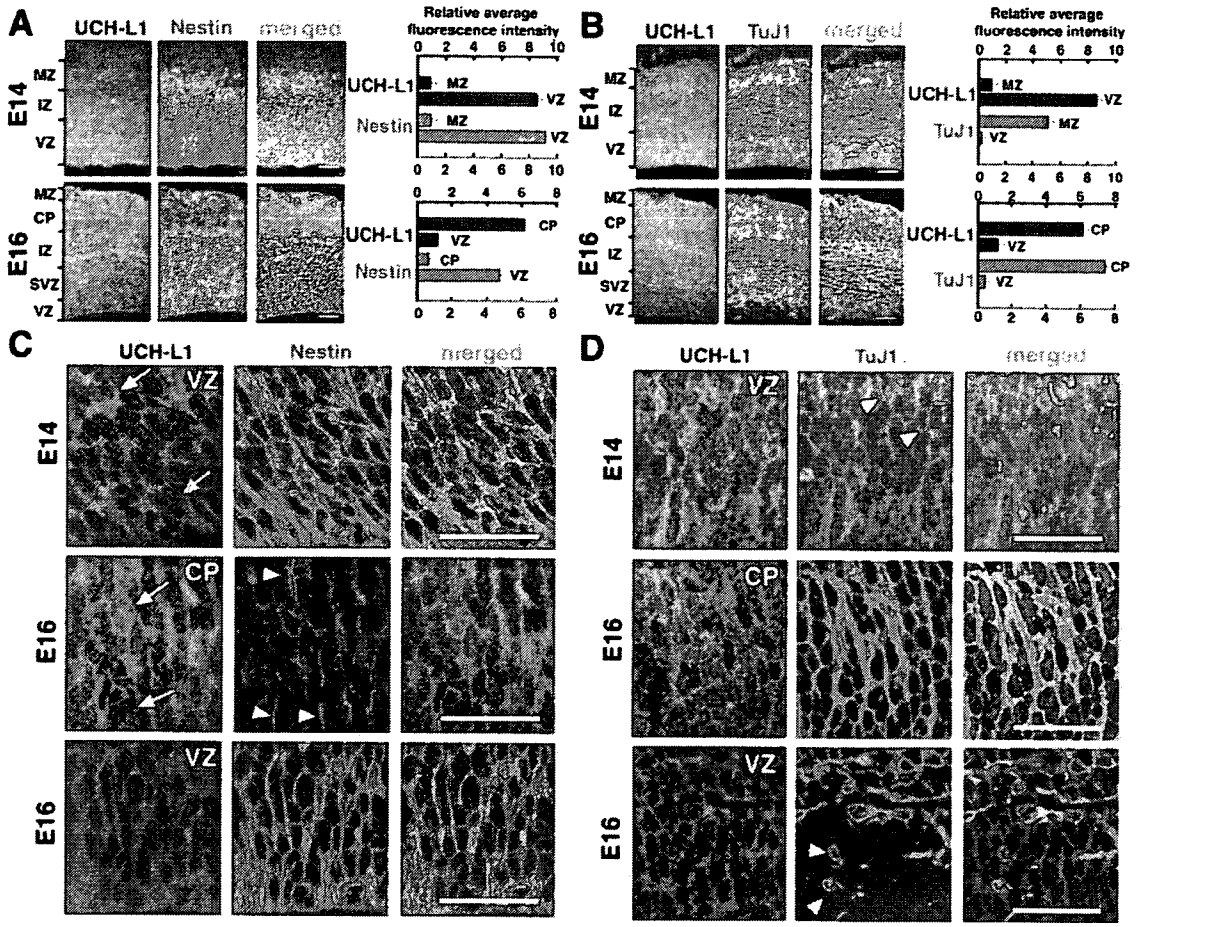

Fig. 2. Change in UCH-L1 expression pattern in the developing mouse brain. Cryosections of the brain at E14 and E16 were double stained with UCH-L1 and the neural progenitor marker nestin (A) or early neuronal marker TuJ1 (B). Unlike with UCH-L1, staining patterns for TuJ1 and nestin do not change between E14 and E16. At E14, UCH-L1 expression is higher in the VZ than in the MZ. At E16, higher expression of UCH-L1 is reciprocally detected in the CP. By contrast, at both E14 and E16, nestin is highly expressed in the VZ, and TuJ1 expression is higher in the MZ/CP. Fluorescence intensities per field (1700 μm^2) were measured in each layer of the E14 and E16 brain and are shown to the right. Bars, 80 μm. (C,D) Higher-magnification images from A,B of UCH-L1 expression in the E14 and E16 brain: UCH-L1 and nestin (C); UCH-L1 and TuJ1 (D). UCH-L1 and nestin are co-expressed in the VZ at E14 and E16. Nestin is expressed only in radial glial fibers (arrowheads) of the CP but not in neurons. UCH-L1 expression level is high. A representative cell with a high level of UCH-LI expression is indicated by a white arrow and one with low expression is indicated by a yellow arrow (C). An early neuronal marker, TuJ1, was expressed in both migrating (arrowheads) and mature neurons (D). CP, cortical plate; IZ, intermediate zone; MZ, marginal zone; SVZ, subventricular zone; VZ, ventricular zone. Bars, 40 μm.

was stronger in the CP than in the VZ at E16 (Fig. 2A,B). The regional change in UCH-L1 expression between E14 and E16 was further confirmed by measuring immunofluorescence intensities from confocal images of the MZ/CP and VZ. At E14, the relative UCH-L1 expression level in the VZ was 9.3 times higher than that in the MZ (Fig. 2A).

Conversely, at E16, when neuronal maturation occurs in the CP, UCH-L1 immunoreactivity in the CP was 5.0 times higher than in the VZ (Fig. 2B). UCH-L1 immunoreactivity colocalized with that of nestin in the VZ at both E14 and E16, although UCH-L1 expression in the VZ was lower at E16 (Fig. 2C). In the VZ at E14, nestin was expressed homogeneously; however, the pattern of UCH-L1 immunoreactivity was mixed, with strong and weak intensities (Fig. 2C; arrow). This expression pattern might reflect the heterogeneity of progenitor cells. Nestin-positive radial glial fibers were observed in the CP at E16 through mature neurons, which strongly expressed UCH-L1 (Fig. 2C) (Malatesta et al., 2000; Malatesta et al., 2003).

UCH-L1 and nestin expression in cultured NPCs

Because areas of nestin and UCH-L1 immunoreactivity overlapped in the VZ, where NPCs reside, we subsequently analyzed the transition of UCH-L1 expression using cultured NPCs. We performed double-labeling experiments for UCH-L1 and nestin expression in cultured NPCs. In the presence of basic fibroblast growth factor (bFGF), when NPCs are proliferating, the percentage of UCH-L1/nestin double-positive

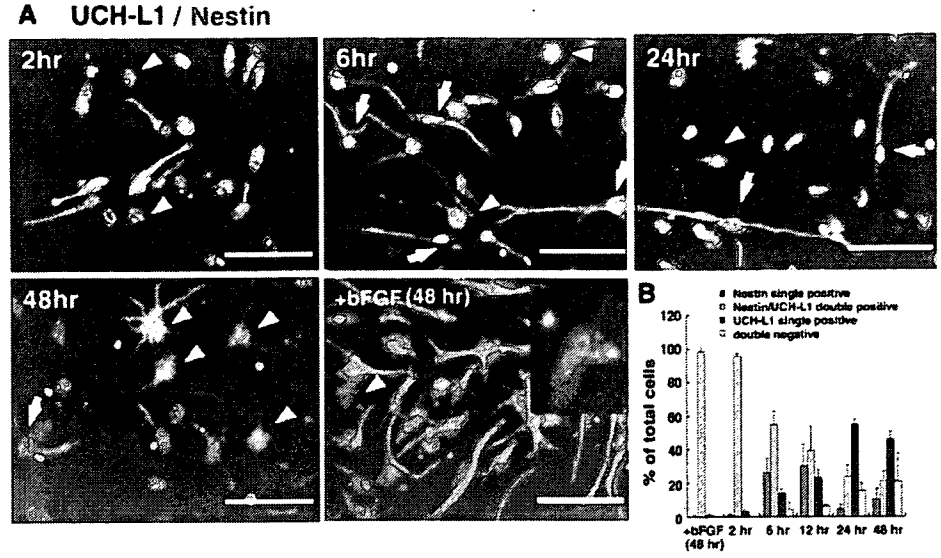

Fig. 3. Nestin and UCH-L1 expression in undifferentiated and differentiating NPCs at 2, 6, 12, 24 and 48 hours. (A) NPCs were immunolabeled with antibodies against nestin and UCH-L1 in the proliferating phase (+bFGF; at 48 hours) or the differentiation phase (–bFGF; 2, 6, 24, 48 hours). Cultures were counterlabeled with Hoechst nuclear dye to facilitate cell quantification. (B) Quantitative analysis of the percentage of cells stained with each antibody. Nestin-positive cells gradually decrease as differentiation proceeds. The UCH-L1 expression level is both high (arrowheads) and low (arrows) in nestin-positive cells at 6 hours. Each experiment was analyzed by counting cells in three independent wells at the indicated times. The experiments were repeated at least two times. Bars, 50 μm.

cells did not change 48 hours after plating, and almost all NPCs expressed UCH-L1 (Fig. 3A). The majority (97.5±2.2%; mean±s.d.) of cultured cells were nestin positive and most of them also stained for UCH-L1 2 hours after plating without bFGF, which triggers NPC differentiation. UCH-L1/nestin double-positive cells were detected at all time points, but as differentiation proceeded their numbers gradually decreased from 95.8±1.9% at 2 hours to 21.5±5.8% at 48 hours (Fig. 3A,B). Although UCH-L1 single-positive cells were rarely detected at 2 hours, the population increased with differentiation, and by 24 hours after bFGF removal 55.1±2.9% of cultured cells were UCH-L1 single-positive cells. Conversely, nestin single-positive cells were readily detected during the earlier phase of differentiation, especially at 6 hours (26.4±8.4% of total cells) and 12 hours (27.0±14.0% of total cells). The differentiating NPCs included nestin-positive cells in which UCH-L1 was either strongly or weakly expressed (Fig. 3A; arrow and arrowhead at 6 hours). These data indicate that UCH-L1 is expressed in progenitor cells as well as in differentiating NPCs. Nestin-positive cells can probably be

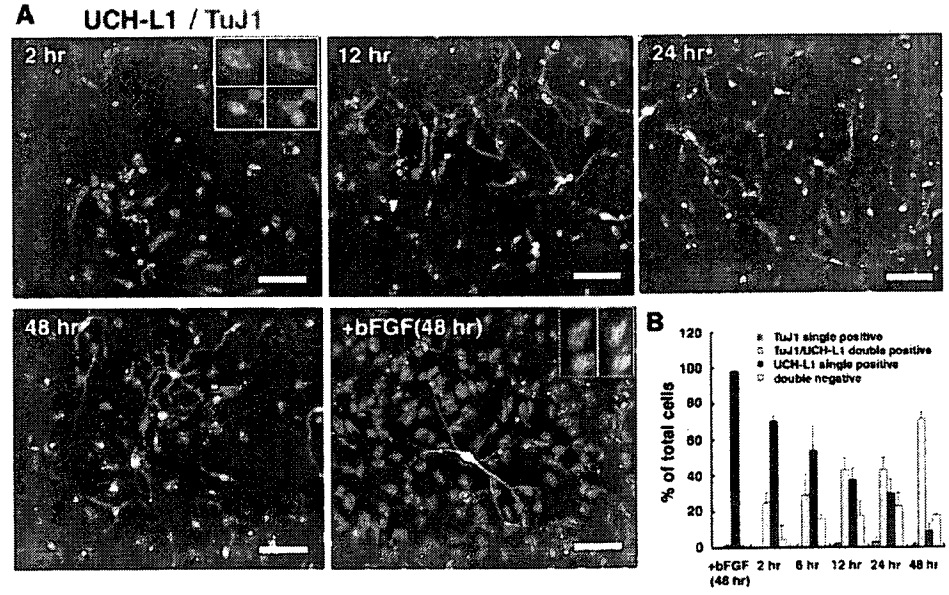

Fig. 4. UCH-L1 expression in neurogenesis. NPCs were immunolabeled with antibodies against TuJ1 and UCH-L1. Cultures were counterlabeled with Hoechst nuclear dye to facilitate cell quantification. Quantitative analysis of the percentage of cells stained with each antibody. (A) In the proliferating phase (+bFGF; at 48 hours) or the differentiation phase (–bFGF; 2, 12, 24, 48 hours), most TuJ1-positive cells co-express UCH-L1. The UCH-L1 expression level is both high and low in TuJ1-positive cells at 48 hours. (B) Quantitative analysis of the percentage of cells stained with each antibody. The number of TuJ1-positive cells gradually increased in the differentiating phase (–bFGF; B). Each experiment was analyzed by counting cells in three independent wells at the indicated times. The experiments were repeated at least two times. Bars, 50 μm.

categorized into at least two subgroups based on their UCH-L1 expression (Fig. 3A,B).

UCH-L1 and TuJ1 expression in cultured NPCs

We then analyzed the expression patterns of UCH-L1 and TuJ1. In the presence of bFGF, TuJ1-positive cells were rarely detected. However, in the absence of bFGF, TuJ1-positive cells were induced. In the cultures without bFGF, as the UCH-L1 single-positive cell population decreased with time, the UCH-L1/TuJ1 double-positive population increased (Fig. 4A,B). UCH-L1/TuJ1 double-negative cells were detected in the differentiating phases at 6, 12, 24 and 48 hours. UCH-L1/TuJ1 double-negative cells might be the nestin single-positive cells at 6 hours and 12 hours in Figs 3 and 4. TuJ1 single-positive cells were infrequently detected in the differentiating NPCs. Because 71.4±3.4% of NPCs differentiated into TuJ1-positive cells under our culture conditions without bFGF at 48 hours, almost all UCH-L1-positive cells are thought to differentiate into TuJ1-positive neuronal cells (Fig. 4A,B). The differentiating NPCs included TuJ1-positive cells in which UCH-L1 was either strongly or weakly expressed (Fig. 4A). These data indicate that UCH-L1-positive NPCs have a high potential for differentiating into neuronal cells and that TuJ1-positive neuronal cells are heterogeneous with regard to UCH-L1 expression.

Morphological classification of UCH-L1-positive NPCs

Nestin is a marker of undifferentiated cells, whereas UCH-L1 is a neuron-specific marker. Here, UCH-L1/nestin double-positive cells were present in cultured NPCs as well as in embryonic brain (Figs 2, 3). Cultured NPCs sequentially gave rise to neurons, then astrocytes, and finally oligodendrocytes (data not shown). Under our culture conditions, neurogenesis actively occurred in differentiating NPCs between 2 and 12 hours after plating (Fig. 4). Glial differentiation had not begun by this time. We collected differentiating NPCs at 6 hours and 12 hours after plating and then analyzed the morphology of nestin-positive cells (Fig. 5). Both UCH-L1/nestin double-positive cells and nestin single-positive cells were present in the population of differentiating NPCs. As the population of double-positive cells might represent a progression of differentiating neurons, we examined the morphology of these cells. Differentiating neurons undergo a stereotypical set of morphological changes, including length (from long to short) (Fukuda et al., 2003; Hartfuss et al., 2003; Nadarajah et al., 2001). We categorized the nestin-positive cells with respect to process length (long, short or round; Fig. 3). UCH-L1 single-positive and double-negative cells were included in the total number of cells. When the total length of processes was more than four times the diameter of the nucleus of the cell, the cell was categorized as 'long', whereas cells with shorter processes were categorized as 'short'. Cells that did not have processes were classified as 'round'. At 6 hours, the majority of nestin single-positive cells were long (18.2±7.6% vs 4.0±0.2% short cells; mean±s.d.; Fisher's PLSD, P=0.008), whereas the majority of UCH-L1/nestin double-positive cells were short (62.0±6.3%). This population was significantly greater than that of long cells (10.3±2.0%) and round cells (5.0±1.7%; Fisher's PLSD, P<0.0001). When NPCs with processes were subcategorized as unipolar, bipolar or multipolar, the unipolar population was significantly higher (62.3±16.9%) than the bipolar population (18.2±3.9%; Fisher's PLSD, P=0.002) in UCH-L1/nestin double-positive cells. Multipolar cells were not observed at 12 hours. However, in nestin single-positive cells, more NPCs were bipolar (16.5±4.6%) than unipolar (4.5±1.9%; Fisher's PLSD, P=0.009; Fig. 6B). Similar results were obtained at 12 hours (Fig. 6). Thus, most UCH-L1/nestin double-positive cells had shorter processes and were more likely to be unipolar.

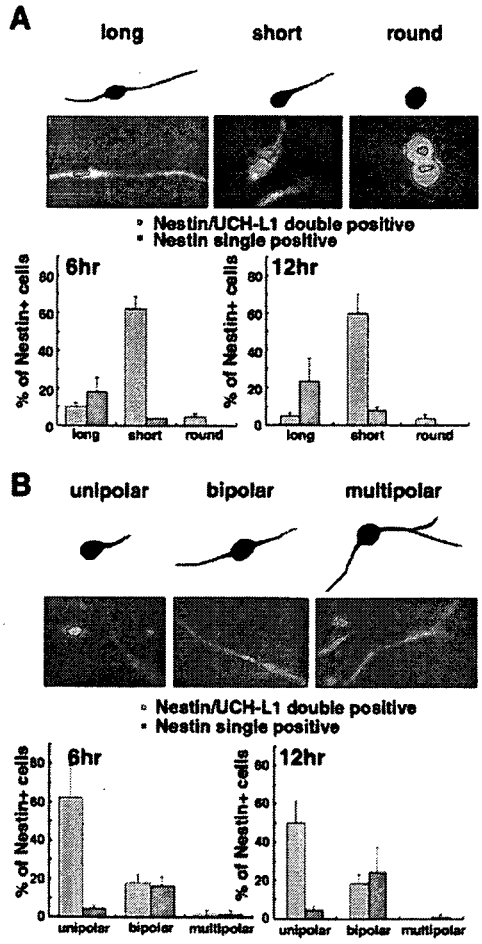

Fig. 5. Morphological identification of subpopulations of cultured NPCs at 6 and 12 hours after induction of differentiation. Differentiating NPCs were double stained with UCH-L1 and nestin. For the quantification depicted in A, differentiating NPCs stained with UCH-L1 and nestin were classified as long, short or round (see text). For the quantification depicted in B, differentiating NPCs were classified based on three kinds of cell morphology: unipolar, bipolar, or multipolar.

Effect of UCH-L1 on nestin-positive processes

We next examined the effect of UCH-L1 on proliferating NPC morphology using the transient transfection method. NPCs were allowed to proliferate for 48 hours after transfection and were then induced to differentiate for 12 hours. The cells were fixed, and the length of nestin-positive processes was examined. To quantify the relationship between UCH-L1 expression and process formation, we measured the total length

of nestin-positive processes. Untransfected NPCs that were nestin positive had mainly long, bipolar processes (Fig. 3A, +bFGF). Cells that were transfected with a green fluorescent protein (GFP) expression vector (negative control) had a morphology that was similar to that of untransfected cells (Fig. 6A). By contrast, cells transfected with wild-type (WT) UCH-L1 cDNA had significantly shorter processes (47.6±6.4 μm, mean±s.e.m., n=81) than mock-transfected cells (69.9±7.0 μm, n=82) (Fig. 6A).

We then examined the relationship between the UCH-L1 structure and its activity with respect to morphological induction. We prepared two UCH-L1 mutants: D30A UCH-L1 lacked hydrolase activity and binding affinity for ubiquitin (Fig. 6B,C) (Osaka et al., 2003); C90S UCH-L1 lacked hydrolase activity but maintained binding affinity for ubiquitin (Fig. 6B,C) (Osaka et al., 2003). We compared the deubiquitylating activity of each UCH-L1 mutant using Ub-AMC as a substrate. The D30A mutant had little hydrolase activity, and the activity of the C90S mutant was not detectable (Fig. 6B; right). Sodium dodecyl sulfate-polyacrylamide gel electrophoresis revealed that there were no detectable contaminating proteins in these recombinant protein preparations (Fig. 6B; left). Co-immunoprecipitation experiments demonstrated that WT UCH-L1 and the C90S mutant physically associated with monoubiquitin. The D30A mutant (as well as GFP alone, which was used as a control) did not associate with ubiquitin (Fig. 6C). Although we did not detect a statistically significant difference, cells transfected with the D30A mutant tended to have longer nestin-positive processes (83.4±7.1 μm, n=87) as compared with cells transfected with the GFP expression vector (Fig. 6A). By contrast, cells transfected with the C90S mutant had significantly shorter fibers (39.3±4.5 μm, n=120; ANOVA: F=11.5, P<0.0001; Dunnett's multiple comparison test: GFP vs WT, P<0.05; GFP vs C90S, P<0.001; GFP vs D30A, P>0.05; Fig. 6A). We also compared the length of nestin-positive processes among UCH-L1 mutants (Bonferroni-Dunn Multiple Comparison Test: WT vs C90S, P=0.32; WT vs D30A, P<0.0001; D30A vs C90S, P<0.0001). Taken together, our data suggest that the effect of UCH-L1 expression on NPC morphology is dependent on the interaction between monoubiquitin and UCH-L1.

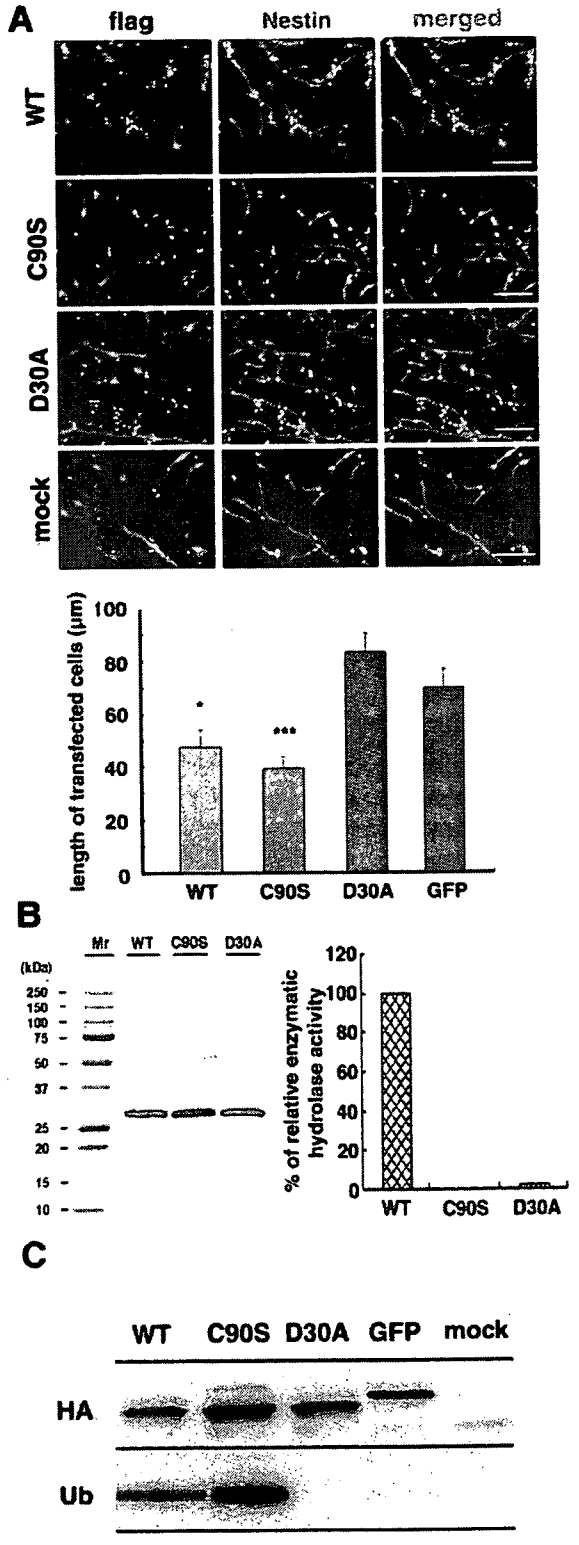

Fig. 6. The induction of short processes depends on the interaction between UCH-L1 and monoubiquitin. (A) FLAG-tagged WT UCH-L1, C90S UCH-L1, D30A UCH-L1 and GFP (all in the pCI-*neo* vector) were transfected into NPCs. Antibodies against the FLAG-tag were used to detect transfected UCH-L1. The green staining shows transfected cells and the red staining shows endogenous nestin. Transient transfection of each construct was performed under proliferating conditions. At 48 hours after transfection, bFGF was removed for 12 hours before the cultures were immunostained. The lengths of nestin-positive processes in immunostained cells were measured. Asterisks indicate differences from the value of GFP-transfected NPCs at *P<0.05 and ***P<0.001. Bars, 80 μm. (B) Visualization of recombinant 6HN-tagged UCH-L1 by sodium dodecyl sulfate-polyacrylamide gel electrophoresis with Coomassie staining (B, left). UCH-L1 hydrolase activity was measured by Ub-AMC hydrolysis. Enzyme concentration was 4.3 nM, and substrate concentration was 700 nM. Initial velocity data was used to determine the values for relative hydrolase activity of UCH-L1 (B, right). (C) UCH-L1 co-immunoprecipitated with Ub. Cytosolic extracts from NIH-3T3 cell lines stably expressing HA-tagged WT UCH-L1 and mutants thereof were immunoprecipitated using anti-HA and immunoblotted with anti-HA antibody or anti-Ub antibody.

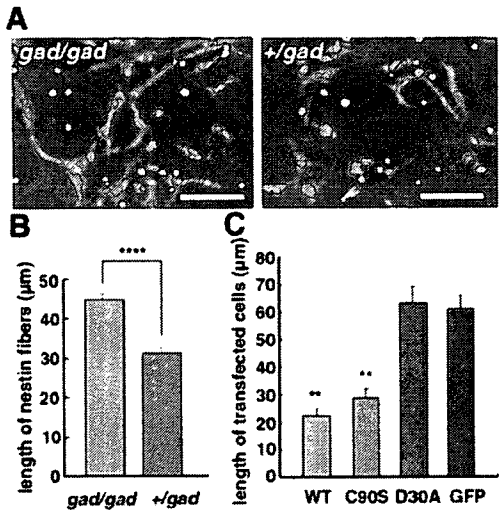

Fig. 7. A comparative experiment of *gad* mice and heterozygous littermates. The experiment compared *gad* mice (A,B) with a transfection study using FLAG-tagged WT UCH-L1, C90S UCH-L1, D30A UCH-L1 and GFP (mock) into *gad*-mouse-derived NPCs (C). The lengths of nestin-positive processes in immunostained cells were measured. NPCs from *gad* mice had longer nestin-positive processes compared with the control (A,B). (C) At 48 hours after transfection, bFGF was removed for 12 hours before the cultures were immunostained. The lengths of nestin-positive processes in immunostained cells were measured. Asterisks indicate differences from the value of GFP-transfected NPCs at $^{**}P<0.01$ and $^{****}P<0.0001$. Bar, 50 μm.

A comparative experiment using *gad*-mouse-derived NPCs

We did a comparative experiment using *gad* mice and heterozygous littermates. Nestin-positive NPCs from *gad* mice had longer processes. When we measured the length of nestin-positive fibers, NPCs from *gad* mice (45.0±1.4 μm, mean±s.e.m., n=366) had significantly longer nestin-positive processes compared with the control (31.4±1.3 μm, n=363) (Mann-Whitney U test: *gad* vs control, $P<0.0001$; Fig. 7A,B).

We next examined the effect of UCH-L1 on *gad*-mouse-derived NPCs using the transient transfection method. As observed in B6-derived cells, NPCs from *gad* mice that were transfected with WT UCH-L1 cDNA had significantly shorter processes (22.2±2.7 μm, mean±s.e.m., n=70) than mock-transfected cells (61.0±4.9 μm, n=88) (Bonferroni-Dunn multiple comparison test: GFP vs WT, $P<0.0001$) (Fig. 7C). Similarly, cells transfected with the C90S mutant had significantly shorter fibers (28.9±3.1 μm, n=71) (GFP vs C90S, $P<0.0001$). Although we did not detect a statistically significant difference, cells transfected with the D30A mutant tended to have longer nestin-positive processes (63.3±5.9 μm, n=80) as compared with cells transfected with the GFP expression vector (GFP vs D30A, P=0.70) (Fig. 7C). We also compared the length of nestin-positive processes among UCH-L1 mutants (Bonferroni-Dunn multiple comparison test: WT vs C90S, P=0.32; WT vs D30A, $P<0.0001$; D30A vs C90S, $P<0.0001$). Taken together, our data suggest that the effect of UCH-L1 expression on NPC morphology is dependent on the interaction between monoubiquitin and UCH-L1.

Discussion

UCH-L1 is a neuron-specific marker in the adult brain. In the present study, we provide experimental evidence that UCH-L1 is expressed in NPCs (Figs 2, 3). Using immunohistochemistry in the mouse brain, we detected UCH-L1 expression at E14 and E16. Interestingly, the expression pattern differed between E14 and E16 (Fig. 2). At E14, when the CP is forming, UCH-L1 expression was higher in the VZ than in the CP. At E14, the VZ contains progenitor cells that are generating neurons in the neocortex (Hashimoto and Mikoshiba, 2004; Malatesta et al., 2003). By contrast, UCH-L1 expression at E16 was lower in the VZ than in the CP. At E16, neuritogenesis and neuronal maturation are active in the CP, and gliogenesis is beginning in the VZ (Rice and Curran, 2001). The cerebral cortex layer becomes thicker at E16, where glial cells are not yet generated. The staining pattern for TuJ1 and nestin did not change between E14 and E16 (Fig. 2), indicating that UCH-L1 is highly expressed in the cortical layer prior to gliogenesis. The change in the expression pattern of UCH-L1 was coincident with the transition from neurogenesis to gliogenesis in the VZ. These results raise the possibility that UCH-L1 mediates not only the neuronal differentiation of NPCs but also the transition from neurogenesis to gliogenesis.

Time is a pivotal factor in the programmed sequence that produces neurons and glial cells from NPCs (Qian et al., 2000), in that the switch from neurogenesis to gliogenesis is regulated by time. The mechanism behind this progression of the progenitor cells is not well understood. Cultured NPCs generate neurons first, followed by astrocytes and then oligodendrocytes (Qian et al., 2000; Temple, 2001). This order of production for each population has been verified in vivo (Sauvageot and Stiles, 2002). The pattern of UCH-L1 immunoreactivity suggests that UCH-L1 is required for the onset of neurogenesis, which is followed by glial differentiation (Fig. 2).

We thus examined the role of UCH-L1 in neurogenesis using cultured NPCs. In UCH-L1/nestin double-staining experiments, the number of double-positive cells decreased with time in culture (Fig. 3). Conversely, UCH-L1 single-positive cells increased. In the double-staining experiments for UCH-L1 and TuJ1, the number of UCH-L1 single-positive cells decreased with time in culture, whereas the number of UCH-L1/TuJ1 double-positive cells increased (Fig. 4). These observations suggest that most UCH-L1-positive cells initially express nestin, but they express TuJ1 at a later stage. As we observed in vivo and in vitro (Figs 2-4), NPCs express UCH-L1, and its expression increases as the NPCs differentiate into neuronal cells. The number of nestin single-positive cells transiently increased before the UCH-L1 single-positive population increased (Fig. 3). The nestin single-positive population might have changed into the UCH-L1/nestin double-negative population (Fig. 3). Although the fate of the double-negative populations remains unknown, the double-negative cells might represent glial cells. Alternatively, some of the nestin single-positive cells might have changed into UCH-L1/nestin double-positive cells and then differentiated into UCH-L1 single-positive cells. A few UCH-L1-negative and TuJ1-positive cells were detected in the differentiating NPCs (Fig. 4). Thus, TuJ1-positive early neurons appear to be heterogeneous. UCH-L1/TuJ1 double-positive immunoreactivity suggested that UCH-L1 is not

absolutely required for some portion of neuronal cell development (Fig. 1B and Fig. 4A). This might explain why *gad* mouse neurons develop despite the absence of UCH-L1.

Because UCH-L1 was expressed in nestin-positive NPCs, we further examined the role of UCH-L1 in cell morphology (Fig. 5). Differentiating NPCs change morphology (Noctor et al., 2001), but the role of UCH-L1 in differentiating neurons has not been investigated. We classified nestin-positive cells based on the length of their processes. Nestin single-positive cells were predominantly long, whereas most UCH-L1/nestin double-positive cells were predominantly short (Fig. 5). These results suggest that UCH-L1 plays a role in regulating NPC process length. We examined this possibility by inducing UCH-L1 in nestin-positive cells. Untransfected, proliferating nestin-positive NPCs had mainly long and bipolar processes [Fig. 3A, bFGF (48 hours)], but when UCH-L1 was transfected, the length of nestin-positive NPC processes shortened (Fig. 6A). The unipolar population increased following UCH-L1 expression. These results support the idea that UCH-L1 regulates NPC morphology. This idea was further confirmed by observations in NPCs from *gad* mice; as shown in Fig. 7B, NPCs from homozygous *gad* mice had longer processes than those from heterozygous controls. In addition, we observed that transfection of UCH-L1 shortened the processes of NPCs from *gad* mice compared with mock transfectants (Fig. 7C).

Our results also suggest that at least two populations of NPCs exist in the embryonic brain. The populations can be classified by the presence or absence of UCH-L1. In the dentate gyrus of the adult mouse brain, there are two distinct subpopulations of nestin-positive cells (Fukuda et al., 2003): those having short processes differentiate into neurons, whereas those having long processes generate late progenitors, which have short processes. The nestin staining pattern of brains from *gad* mice differed from that of brains from heterozygous littermates (Fig. 1). In the *gad* mouse brain, nestin-positive radial fibers were prominent, and almost all progenitor cells appeared to have long processes (Fig. 1). Since UCH-L1 affected NPC morphology (Fig. 6A and Fig. 7C), the difference in vivo indicates that differentiation itself was modulated by the absence of UCH-L1. Considering that neurons are present in the *gad* mouse even though it lacks UCH-L1 expression, further investigation into the morphological role of UCH-L1 using various approaches including the BrdU studies should provide important information about the heterogeneity of cortical neurons.

UCHs hydrolyze ubiquitin C-terminal small adducts in vitro (Larsen et al., 1998). Recently, a significant relationship was reported between UCH-L1 hydrolase activity and cell proliferation in lung cancer cell lines (Liu et al., 2003). We previously demonstrated that UCH-L1 extends ubiquitin half-life and prevents ubiquitin degradation. This function depends on the interaction between UCH-L1 and monoubiquitin but not on hydrolase activity (Osaka et al., 2003). In the present study, WT UCH-L1 and the C90S mutant both decreased the length of NPC processes. Both molecules associate with monoubiquitin, unlike another mutant, D30A, which did not affect process length (Fig. 6). Similar results were obtained from the transfection study using nestin-positive NPCs from *gad* mice (Fig. 7C). Thus, the effect of UCH-L1 on NPC process length is dependent on the interaction between UCH-L1 and ubiquitin but not on hydrolase activity. Although we did not examine the ligase activity of each mutant (Liu et al., 2002), the C90S mutant is unlikely to have ligase activity, because conjugation of ubiquitin to the C90S mutant forms a stable complex that prevents the release of ubiquitin (Sullivan and Vierstra, 1993). This observation suggests that the ligase activity is not related to the morphological changes that occurred in NPCs.

The ubiquitin system has an essential role in various physiological events, including cell-cycle progression, specific gene transcription, membrane protein trafficking, reversal of stress damage and intracellular signaling (Weissman, 2001). In cortical neurogenesis, the role of the ubiquitin system is not well understood. Several molecules that are important in cortical neurogenesis, including Notch, P35 and Dab1, are ubiquitylated (Arnaud et al., 2003; Bock et al., 2004; Patrick et al., 1998; Qiu et al., 2000). Here we show for the first time that UCH-L1 is expressed in NPCs and regulates their morphology. In addition, in vivo UCH-L1 expression is localized to the VZ and cortical layers that are undergoing neurogenesis. Cells undergoing gliogenesis had little UCH-L1 expression in vivo. These results suggest that UCH-L1 facilitates neurogenesis, an activity that appears to depend on the affinity of UCH-L1 for ubiquitin.

Materials and Methods

Animals

Pregnant C57BL/6J mice were purchased from CLEA Japan. The *gad* mouse is an autosomal recessive mutant that was obtained by crossing CBA and RFM mice (Saigoh et al., 1999). The *gad* line was maintained by intercrossing for more than 20 generations (Kwon et al., 2003; Saigoh et al., 1999). All animal experiments were performed in the laboratory according to the NIH Standards for Treatment of Laboratory Animals.

Antibodies and reagents

Monoclonal and polyclonal antibodies used in this study were as follows: monoclonal anti-nestin antibody (Becton Dickinson; and Rat401, Developmental Studies Hybridoma Bank, The University of Iowa, Iowa City, IA), monoclonal anti-neuronal tubulin β III antibody (TuJ1; Covance), polyclonal anti-UCH-L1 antibody (PGP9.5; RA95101, UltraClone), and polyclonal anti-FLAG antibody (Sigma). All secondary polyclonal antibodies conjugated to Alexa Fluor fluorescein were purchased from Molecular Probes.

Cortical NPC culture and differentiation conditions in C57BL/6 mice

Cortical NPCs were cultured as previously described (Nakashima et al., 1999). Briefly, embryos were removed from pregnant C57BL/6J mice (CLEA Japan) and staged according to morphological criteria to confirm the gestational day (Kaufman et al., 1998). Developing mouse cerebral cortex was dissected from E14 embryos. Cells were mechanically dissociated by trituration and plated at a concentration of 3.0×10^6 cells per 10 cm dish (Becton Dickinson) precoated with 10 ml of 15 μg/ml poly-L-ornithine (Sigma) and 10 ml of 1 μg/ml fibronectin (Nitta Gelatin). Cells were expanded for 5 days in serum-free neurobasal (NB) medium (Invitrogen) supplemented with B27 (Invitrogen), 0.5 mM L-glutamine (Invitrogen), 100 U/ml penicillin and 100 μg/ml streptomycin (Invitrogen). This medium contained 10 ng/ml bFGF (PeproTech). Cultures were maintained at 37°C in an atmosphere of 95% air and 5% CO_2. For secondary culture, bFGF-expanded NPCs were washed in warm Hank's Balanced Salt Solution, detached with mechanical pipetting, and resuspended in NB medium supplemented with B27, but not bFGF. Cells were then replated in 24-well plates (Nunc: 1.8×10^5 cells per well) that were precoated with 500 μl of 15 μg/ml poly-L-ornithine and 500 μl of 1 μg/ml fibronectin for immunofluorescence staining at each time point.

Cortical NPC culture and differentiation conditions in *gad* mice

Culture of NPCs derived from *gad* mice was performed as with NPCs derived from B6 mice. Developing mouse cerebral cortex was dissected from embryos at E13.5 to E14.5. The precise gestational day was determined according to previously established morphological criteria (Kaufman et al., 1998). NPCs from each embryo were collected and cultured separately. Each genotype was determined later using PCR and, as a result, each pair of *gad* and control littermate mice from two sets of

parents were used. Each culture of NPCs was replated in 24-well plates without bFGF and stained using anti-UCH-L1 24 hours after plating.

Immunohistochemistry

Brain sections were stained as previously described (Li et al., 2003; Osaka et al., 2003). Briefly, E14 and E16 mouse brains were removed and fixed in 4% paraformaldehyde/phosphate-buffered saline (PBS) for 2 hours at room temperature, cryoprotected in 30% sucrose in PBS and frozen in dry ice. Sections (20 μm thick) were cut on a cryostat, and mounted on aminopropylsilane (APS)-coated glass slides. They were then washed three times in PBS for 5 minutes, and blocked for 1 hour at room temperature with 3% bovine serum albumin, 2% (v/v) normal goat serum, and 0.2% (v/v) Triton X-100 in PBS (pH 7.4). Sections were incubated with primary antibodies [anti-nestin antibody (Rat401) 1:10; or anti-UCH-L1 antibody (RA95101) 1:4000; or anti-TuJ1 antibody, 1:1000] overnight at 4°C or for 2 hours at room temperature. After rinsing in PBS, the sections were incubated for 2 hours with diluted fluorescein-conjugated secondary antibody (1:200). The images were obtained with a confocal laser scanning TCS SL microscope, and detailed analyses were performed using an LSC confocal microscope system (Leica). Immunofluorescence intensities were measured from confocal images with Mac SCOPE software (version 2.59; Mitani).

Immunocytochemistry

Cells were stained as previously described (Aoki et al., 2002). Briefly, all incubations and washes were performed at room temperature. Cells were fixed with 3.8% formaldehyde/PBS for 10 minutes and permeabilized with 0.02% (v/v) Triton X-100/PBS for 5 minutes. Fixed cells were blocked with 3.3% goat serum for 30 minutes. Cells were incubated with a diluted primary polyclonal or monoclonal antibody (both were used for double staining) for 0.5-1 hour. The cells were then incubated with diluted secondary antibody conjugated to fluorescein for 0.5-1 hour. Antibody dilutions were as follows: anti-UCH-L1 antibody, 1:4000; anti-nestin antibody, 1:500; anti-TuJ1, 1:500. All secondary antibodies were diluted 1:200 in 1% goat serum/PBS before use. The images were obtained with fluorescence microscopy on an IX70 microscope (Olympus).

Transfection

For C57BL/6 mice, cells replated in 24-well plates were cultured overnight in growth medium containing bFGF and B27. The next day, each construct was transfected using Lipofectamine 2000 (Invitrogen) according to the manufacturer's instructions. NPCs were allowed to proliferate for 48 hours after transfection and then induced to differentiate for 12 hours without bFGF. For *gad*-mouse-derived NPCs, transfection was done in a similar manner.

Expression plasmids for human UCH-L1 variants

Mutant cDNAs encoding human UCH-L1 containing either the D30A or C90S substitution were obtained using the QuikChange site-directed mutagenesis kit (Stratagene) with the following mutagenesis oligonucleotides: 5′-CAGTGG-CGCTTCGTGGCCGTGCTGGGGCTGGAAG-3′ and 5′-CTTCCAGCCCCAG-CACGGCCACGAAGCGCCACTG-3′ for D30A; 5′-CCATTGGGAATTCCTCT-GGCACAATCGGAC-3′ and 5′-GTCCGATTGTGCCACAGGAATTCCCAA-TGG-3′ for C90S. Each single-nucleotide mutation in the resulting plasmids was confirmed by sequencing. Mammalian expression plasmids containing either FLAG-tagged human WT UCH-L1 or the D30A or C90S mutants were constructed using a pCI-*neo* mammalian expression vector (Promega). Bacterial expression plasmids containing either 6HN-tagged human WT UCH-L1 or the D30A or C90S mutants were constructed using a tetracycline-inducible expression system. *Xho*I-*Not*I cDNA fragments of the pCI-*neo* WT UCH-L1 or the D30A and C90S mutants and constructs were digested, and the DNA fragments were ligated between the *Sal*I and *Not*I sites in pPROtetE233 (Clontech) to generate pPROtetE233 6HN-tagged human WT, D30A and C90S UCH-L1 vectors. These expression plasmids were confirmed by sequencing.

In vitro assay for human UCH-L1 activity

Purified human UCH-L1 and the fluorogenic substrate ubiquitin-7-amino-4-methylcoumarin (Ub-AMC; Boston Biochem) were used to determine steady-state kinetic parameters as described previously (Nishikawa et al., 2003).

Immunoprecipitation

NIH-3T3 cells stably expressing human WT UCH-L1 or the C90S or D30A mutants, all with an HA-FLAG double tag at the N terminus, were cultured to subconfluency in a 10 cm dish, lyzed with 1 ml of modified RIPA buffer [50 mM Tris-HCl, pH 7.5, 1% (v/v) NP-40, 0.25% sodium deoxycholate, 150 mM NaCl, 1 mM EDTA] with EDTA-free complete protease inhibitor cocktail (Roche), sonicated and centrifuged at 18,000 *g* for 20 minutes at 4°C. Immunoprecipitation was performed as described previously (Ogawa et al., 2002).

Statistics

Statistical analyses were performed using StatView, version 5.0 (SAS) and Prism, version 3 (GraphPad Software). Analysis of variance (ANOVA) was used to assess differences between groups. A P value of less than 0.05 was considered statistically significant. When ANOVA results were statistically significant, they were examined by Fisher's PLSD, or Dunnett's multiple comparison test, or Bonferroni-Dunn multiple comparisons post hoc test. Differences between *gad* mice and control mice were analyzed using the Mann-Whitney U test.

The authors thank Yuh Nung Jan and Hua-Shun Li for providing the immunohistochemistry methods; Yoshihiro Nakatani and Hidesato Ogawa for providing the retroviral expression system and immunoprecipitation methods; and Masako Shikama for the care and breeding of animals. This work was supported by Grants-in-Aid for Scientific Research from the Ministry of Health, Labour and Welfare of Japan, and Grants-in-Aid for Scientific Research from the Ministry of Education, Culture, Sports, Science and Technology of Japan.

References

Aoki, S., Su, Q., Li, H., Nishikawa, K., Ayukawa, K., Hara, Y., Namikawa, K., Kiryu-Seo, S., Kiyama, H. and Wada, K. (2002). Identification of an axotomy-induced glycosylated protein, AIGP1, possibly involved in cell death triggered by endoplasmic reticulum-Golgi stress. *J. Neurosci.* **22**, 10751-10760.

Arnaud, L., Ballif, B. A. and Cooper, J. A. (2003). Regulation of protein tyrosine kinase signaling by substrate degradation during brain development. *Mol. Cell. Biol.* **23**, 9293-9302.

Bock, H. H., Jossin, Y., May, P., Bergner, O. and Herz, J. (2004). Apolipoprotein E receptors are required for reelin-induced proteasomal degradation of the neuronal adaptor protein Disabled-1. *J. Biol. Chem.* **279**, 33471-33479.

Dickson, D. W., Schmidt, M. L., Lee, V. M., Zhao, M. L., Yen, S. H. and Trojanowski, J. Q. (1994). Immunoreactivity profile of hippocampal CA2/3 neurites in diffuse Lewy body disease. *Acta Neuropathol. (Berl.)* **87**, 269-276.

Fukuda, S., Kato, F., Tozuka, Y., Yamaguchi, M., Miyamoto, Y. and Hisatsune, T. (2003). Two distinct subpopulations of nestin-positive cells in adult mouse dentate gyrus. *J. Neurosci.* **23**, 9357-9366.

Hartfuss, E., Forster, E., Bock, H. H., Hack, M. A., Leprince, P., Luque, J. M., Herz, J., Frotscher, M. and Gotz, M. (2003). Reelin signaling directly affects radial glia morphology and biochemical maturation. *Development* **130**, 4597-4609.

Hashimoto, M. and Mikoshiba, K. (2004). Neuronal birthdate-specific gene transfer with adenoviral vectors. *J. Neurosci.* **24**, 286-296.

Kaufman, M. H., Brune, R. M., Davidson, D. R. and Baldock, R. A. (1998). Computer-generated three-dimensional reconstructions of serially sectioned mouse embryos. *J. Anat.* **193**, 323-336.

Kawauchi, T., Chihama, K., Nabeshima, Y. and Hoshino, M. (2003). The in vivo roles of STEF/Tiam1, Rac1 and JNK in cortical neuronal migration. *EMBO J.* **22**, 4190-4201.

Kwon, J., Kikuchi, T., Setsuie, R., Ishii, Y., Kyuwa, S. and Yoshikawa, Y. (2003). Characterization of the testis in congenitally ubiquitin carboxy-terminal hydrolase-1 (Uch-L1) defective (gad) mice. *Exp. Anim.* **52**, 1-9.

Larsen, C. N., Krantz, B. A. and Wilkinson, K. D. (1998). Substrate specificity of deubiquitinating enzymes: ubiquitin C-terminal hydrolases. *Biochemistry* **37**, 3358-3368.

Leroy, E., Boyer, R., Auburger, G., Leube, B., Ulm, G., Mezey, E., Harta, G., Brownstein, M. J., Jonnalagada, S., Chernova, T. et al. (1998). The ubiquitin pathway in Parkinson's disease. *Nature* **395**, 451-452.

Li, H. S., Wang, D., Shen, Q., Schonemann, M. D., Gorski, J. A., Jones, K. R., Temple, S., Jan, L. Y. and Jan, Y. N. (2003). Inactivation of Numb and Numblike in embryonic dorsal forebrain impairs neurogenesis and disrupts cortical morphogenesis. *Neuron* **40**, 1105-1118.

Liu, Y., Fallon, L., Lashuel, H. A., Liu, Z. and Lansbury, P. T., Jr (2002). The UCH-L1 gene encodes two opposing enzymatic activities that affect alpha-synuclein degradation and Parkinson's disease susceptibility. *Cell* **111**, 209-218.

Liu, Y., Lashuel, H. A., Choi, S., Xing, X., Case, A., Ni, J., Yeh, L. A., Cuny, G. D., Stein, R. L. and Lansbury, P. T., Jr (2003). Discovery of inhibitors that elucidate the role of UCH-L1 activity in the H1299 lung cancer cell line. *Chem. Biol.* **10**, 837-846.

Malatesta, P., Hartfuss, E. and Gotz, M. (2000). Isolation of radial glial cells by fluorescent-activated cell sorting reveals a neuronal lineage. *Development* **127**, 5253-5263.

Malatesta, P., Hack, M. A., Hartfuss, E., Kettenmann, H., Klinkert, W., Kirchhoff, F. and Gotz, M. (2003). Neuronal or glial progeny: regional differences in radial glia fate. *Neuron* **37**, 751-764.

McQuaid, S., McConnell, R., McMahon, J. and Herron, B. (1995). Microwave antigen retrieval for immunocytochemistry on formalin-fixed, paraffin-embedded post-mortem CNS tissue. *J. Pathol.* **176**, 207-216.

Nadarajah, B., Brunstrom, J. E., Grutzendler, J., Wong, R. O. and Pearlman, A. L. (2001). Two modes of radial migration in early development of the cerebral cortex. *Nat. Neurosci.* **4**, 143-150.

Nakashima, K., Yanagisawa, M., Arakawa, H., Kimura, N., Hisatsune, T., Kawabata, M., Miyazono, K. and Taga, T. (1999). Synergistic signaling in fetal brain by STAT3-Smad1 complex bridged by p300. *Science* **284**, 479-482.

Nishikawa, K., Li, H., Kawamura, R., Osaka, H., Wang, Y. L., Hara, Y., Hirokawa, T., Manago, Y., Amano, T., Noda, M. et al. (2003). Alterations of structure and

hydrolase activity of parkinsonism-associated human ubiquitin carboxyl-terminal hydrolase L1 variants. *Biochem. Biophys. Res. Commun.* **304**, 176-183.

Noctor, S. C., Flint, A. C., Weissman, T. A., Dammerman, R. S. and Kriegstein, A. R. (2001). Neurons derived from radial glial cells establish radial units in neocortex. *Nature* **409**, 714-720.

Noctor, S. C., Flint, A. C., Weissman, T. A., Wong, W. S., Clinton, B. K. and Kriegstein, A. R. (2002). Dividing precursor cells of the embryonic cortical ventricular zone have morphological and molecular characteristics of radial glia. *J. Neurosci.* **22**, 3161-3173.

Noctor, S. C., Martinez-Cerdeno, V., Ivic, L. and Kriegstein, A. R. (2004). Cortical neurons arise in symmetric and asymmetric division zones and migrate through specific phases. *Nat. Neurosci.* **7**, 136-144.

Ogawa, H., Ishiguro, K., Gaubatz, S., Livingston, D. M. and Nakatani, Y. (2002). A complex with chromatin modifiers that occupies E2F- and Myc-responsive genes in G0 cells. *Science* **296**, 1132-1136.

Osaka, H., Wang, Y. L., Takada, K., Takizawa, S., Setsuie, R., Li, H., Sato, Y., Nishikawa, K., Sun, Y. J., Sakurai, M. et al. (2003). Ubiquitin carboxy-terminal hydrolase L1 binds to and stabilizes monoubiquitin in neuron. *Hum. Mol. Genet.* **12**, 1945-1958.

Patrick, G. N., Zhou, P., Kwon, Y. T., Howley, P. M. and Tsai, L. H. (1998). p35, the neuronal-specific activator of cyclin-dependent kinase 5 (Cdk5) is degraded by the ubiquitin-proteasome pathway. *J. Biol. Chem.* **273**, 24057-24064.

Qian, X., Goderie, S. K., Shen, Q., Stern, J. H. and Temple, S. (1998). Intrinsic programs of patterned cell lineages in isolated vertebrate CNS ventricular zone cells. *Development* **125**, 3143-3152.

Qian, X., Shen, Q., Goderie, S. K., He, W., Capela, A., Davis, A. A. and Temple, S. (2000). Timing of CNS cell generation: a programmed sequence of neuron and glial cell production from isolated murine cortical stem cells. *Neuron* **28**, 69-80.

Qiu, L., Joazeiro, C., Fang, N., Wang, H. Y., Elly, C., Altman, Y., Fang, D., Hunter, T. and Liu, Y. C. (2000). Recognition and ubiquitination of Notch by Itch, a hect-type E3 ubiquitin ligase. *J. Biol. Chem.* **275**, 35734-35737.

Rice, D. S. and Curran, T. (2001). Role of the reelin signaling pathway in central nervous system development. *Annu. Rev. Neurosci.* **24**, 1005-1039.

Roegiers, F. and Jan, Y. N. (2004). Asymmetric cell division. *Curr. Opin. Cell Biol.* **16**, 195-205.

Saigoh, K., Wang, Y. L., Suh, J. G., Yamanishi, T., Sakai, Y., Kiyosawa, H., Harada, T., Ichihara, N., Wakana, S., Kikuchi, T. et al. (1999). Intragenic deletion in the gene encoding ubiquitin carboxy-terminal hydrolase in gad mice. *Nat. Genet.* **23**, 47-51.

Satoh, J. and Kuroda, Y. (2001). A polymorphic variation of serine to tyrosine at codon 18 in the ubiquitin C-terminal hydrolase-L1 gene is associated with a reduced risk of sporadic Parkinson's disease in a Japanese population. *J. Neurol. Sci.* **189**, 113-117.

Sauvageot, C. M. and Stiles, C. D. (2002). Molecular mechanisms controlling cortical gliogenesis. *Curr. Opin. Neurobiol.* **12**, 244-249..

Schofield, J. N., Day, I. N., Thompson, R. J. and Edwards, Y. H. (1995). PGP9.5, a ubiquitin C-terminal hydrolase: pattern of mRNA and protein expression during neural development in the mouse. *Brain Res. Dev. Brain Res.* **85**, 229-238.

Sekiguchi, S., Yoshikawa, Y., Tanaka, S., Kwon, J., Ishii, Y., Kyuwa, S., Wada, K., Nakamura, S. and Takahashi, K. (2003). Immunohistochemical analysis of protein gene product 9.5, a ubiquitin carboxyl-terminal hydrolase, during placental and embryonic development in the mouse. *Exp. Anim.* **52**, 365-369.

Shen, Q., Qian, X., Capela, A. and Temple, S. (1998). Stem cells in the embryonic cerebral cortex: their role in histogenesis and patterning. *J. Neurobiol.* **36**, 162-174.

Sullivan, M. L. and Vierstra, R. D. (1993). Formation of a stable adduct between ubiquitin and the Arabidopsis ubiquitin-conjugating enzyme, AtUBC1+. *J. Biol. Chem.* **268**, 8777-8780.

Tabata, H. and Nakajima, K. (2003). Multipolar migration: the third mode of radial neuronal migration in the developing cerebral cortex. *J. Neurosci.* **23**, 9996-10001.

Temple, S. (2001). The development of neural stem cells. *Nature* **414**, 112-117.

Weissman, A. M. (2001). Themes and variations on ubiquitylation. *Nat. Rev. Mol. Cell. Biol.* **2**, 169-178.

Wilkinson, K. D., Lee, K. M., Deshpande, S., Duerksen-Hughes, P., Boss, J. M. and Pohl, J. (1989). The neuron-specific protein PGP 9.5 is a ubiquitin carboxyl-terminal hydrolase. *Science* **246**, 670-673.

Zhong, W., Feder, J. N., Jiang, M. M., Jan, L. Y. and Jan, Y. N. (1996). Asymmetric localization of a mammalian numb homolog during mouse cortical neurogenesis. *Neuron* **17**, 43-53.

Zhong, W., Jiang, M. M., Weinmaster, G., Jan, L. Y. and Jan, Y. N. (1997). Differential expression of mammalian Numb, Numblike and Notch1 suggests distinct roles during mouse cortical neurogenesis. *Development* **124**, 1887-1897.

MOLECULAR AND CELLULAR BIOLOGY, Sept. 2006, p. 6923–6935 Vol. 26, No. 18
0270-7306/06/$08.00+0 doi:10.1128/MCB.02474-05

Solo/Trio8, a Membrane-Associated Short Isoform of Trio, Modulates Endosome Dynamics and Neurite Elongation

Ying-Jie Sun,[1,5]† Kaori Nishikawa,[1,3]† Hideki Yuda,[1] Yu-Lai Wang,[1] Hitoshi Osaka,[3] Nobuna Fukazawa,[1,4] Akira Naito,[5] Yoshihisa Kudo,[4] Keiji Wada,[1,7] and Shunsuke Aoki[1,2,6,7]*

Department of Degenerative Neurological Diseases[1] and Department of Demyelinating Disease and Aging,[2] National Institute of Neuroscience, NCNP, Kodaira, Tokyo 187-8502, Japan; Japan Science and Technology Agency (JST), Kawaguchi, Saiatama 332-0012, Japan[3]; Laboratory of Cellular Neurobiology, Tokyo University of Pharmacology and Life Science, Hachioji, Tokyo 192-0392, Japan[4]; Department of Anatomy and Structural Science, Yamagata University School of Medicine, Yamagata 990-9585, Japan[5]; New Energy and Industrial Technology Development Organization (NEDO), Kawasaki, Kanagawa 212-8554, Japan[6]; and JST,CREST, Kawaguchi, Saitama 332-0012, Japan[7]

Received 28 December 2005/Returned for modification 15 February 2006/Accepted 28 June 2006

With DNA microarrays, we identified a gene, termed *Solo*, that is downregulated in the cerebellum of Purkinje cell degeneration mutant mice. Solo is a mouse homologue of rat Trio8—one of multiple Trio isoforms recently identified in rat brain. Solo/Trio8 contains N-terminal sec14-like and spectrin-like repeat domains followed by a single guanine nucleotide exchange factor 1 (GEF1) domain, but it lacks the C-terminal GEF2, immunoglobulin-like, and kinase domains that are typical of Trio. Solo/Trio8 is predominantly expressed in Purkinje neurons of the mouse brain, and expression begins following birth and increases during Purkinje neuron maturation. We identified a novel C-terminal membrane-anchoring domain in Solo/Trio8 that is required for enhanced green fluorescent protein-Solo/Trio8 localization to early endosomes (positive for both early-endosome antigen 1 [EEA1] and Rab5) in COS-7 cells and primary cultured neurons. Solo/Trio8 overexpression in COS-7 cells augmented the EEA1-positive early-endosome pool, and this effect was abolished via mutation and inactivation of the GEF domain or deletion of the C-terminal membrane-anchoring domain. Moreover, primary cultured neurons transfected with Solo/Trio8 showed increased neurite elongation that was dependent on these domains. These results suggest that Solo/Trio8 acts as an early-endosome-specific upstream activator of Rho family GTPases for neurite elongation of developing Purkinje neurons.

Endosomal membrane trafficking in neurons plays a key role in various neural processes, including neurite elongation (19, 33), synaptic transmission (17), neuronal degeneration (36), and neuronal cell death or survival (7). The early endosome regulates the selective transfer of membrane proteins to other organelles, and thus it is a key organelle for sorting vesicles containing cell surface membrane proteins, including receptors, transporters, channels, and cell adhesion molecules (2, 29, 39, 47).

Several lines of evidence suggest that small GTPases play pivotal roles in regulating early-endosome dynamics (2, 39, 47). For example, Rab5 regulates the motility and fusion of early endosomes (32), whereas Rab4 and Rab5 control vesicle influx and efflux, respectively, in the early-endosome pool (28). Rho family GTPases also regulate early-endosome dynamics. Once such GTPase, Cdc42, controls endocytic transport in polarized cells (20), whereas RhoD specifically localizes to early endosomes and regulates their motility via diaphanous-related formin proteins (13). Upstream regulators of small GTPases that associate with early endosomes have been studied extensively. For example, early-endosome antigen 1 (EEA1) acts as an effector for Rab family small GTPases (5, 45). Although Rho family GTPases are also activated by multivalent upstream effectors (42), the specialized upstream activators that function in early endosomes remain unknown.

Trio, a member of the Dbl homology domain family of guanine nucleotide exchange factors (GEFs), was originally identified by its interaction with the leukocyte common antigen-related protein receptor (6). Trio has an N-terminal sec14-like domain, spectrin-like repeats, two GEF domains (GEF1 and GEF2), an immunoglobulin (Ig)-like domain, and a C-terminal Ser/Thr kinase domain (3). The GEF1 domain activates RhoG and Rac1, whereas GEF2 acts on RhoA, suggesting that Trio is involved in multiple GTPase cascades mediating various cellular processes (3). Genetic analysis of the Trio gene in *Drosophila* embryos implicates this protein in neuronal and retinal axon guidance (3). Mice lacking Trio die during embryogenesis and exhibit a loss of myofiber formation and cellular disorganization in the hippocampus and olfactory bulb (35). Although Trio is highly expressed in the adult brain, heart, liver, skeletal muscle, kidney, placenta, and pancreas (6), its effector function in these adult tissues remains unknown. Several Trio isoforms were recently identified (25), and the expression of each isoform was shown to be regulated in a tissue-specific manner. The functions of these isoforms, however, have not been delineated.

Purkinje cell degeneration (pcd) is an autosomal recessive

* Corresponding author. Mailing address: Department of Degenerative Neurological Diseases, National Institute of Neuroscience, National Center of Neurology and Psychiatry, 4-1-1 Ogawahigashi, Kodaira, Tokyo 187-8502, Japan. Phone: 81-42-346-1715. Fax: 81-42-346-1745. E-mail: aokis@ncnp.go.jp.

† Y.-J.S. and K.N. contributed equally to this work.

mutational disorder in mice that is characterized by degenerative loss of Purkinje neurons after postnatal day 15 (P15) to P18 (30). The causative mutation of pcd was identified at the *Nna1* locus (12). The disorder constitutes an adult-onset disease and presents mild phenotypes, thereby facilitating the analysis of cerebella that are nearly devoid of Purkinje neurons. Thus, the pcd mouse has been repeatedly used to screen for Purkinje neuron-specific genes, such as the gene encoding 28-kDa calbindin (34) or inositol 3-phosphate receptor 1 (IP3R) (24).

In this study, we used DNA microarrays to analyze gene expression in the cerebella of mice carrying a mutation governing pcd (30). We identified a Purkinje-predominant mouse cDNA encoding the protein Solo, which is a membrane-associated isoform of Trio. Amino acid sequence analysis showed that Solo is a homologue of the recently identified rat protein Trio8 (25). Solo/Trio8 specifically localized to early endosomes and regulated their dynamics. We also found that Solo/Trio8 modulated neurite morphology in primary cultured neurons. These data suggest that Solo/Trio8 is involved in the development of Purkinje neurons by affecting the dynamics of early endosomes.

MATERIALS AND METHODS

Animals. C57BL/6J-pcd mice were obtained from The Jackson Laboratory (Bar Harbor, ME). The cerebella of P24 pcd and wild-type (WT) mice were used for DNA microarrays. For SYBR green-based real-time quantitative reverse transcription (RT)-PCR, three cerebella were collected on each postnatal day. Animal care and handling were in accordance with institutional regulations for animal care and public law and were approved by the Animal Investigation Committee of the National Institute of Neuroscience, Japan.

DNA microarrays. Equivalent amounts of total RNA derived from each cerebellar sample were reverse transcribed into double-stranded cDNA that was then used as a template to synthesize biotin-labeled cRNA with the BioArray HighYield RNA transcription labeling kit (Enzo Diagnostics, Farmingdale, NY). Labeled cRNA was purified on RNeasy affinity resin (QIAGEN, Valencia, CA) and fragmented randomly to an average size of 50 to 100 bases by incubation in 40 mM Tris-acetate, pH 8.2, containing 100 mM K-acetate and 30 mM Mg-acetate at 94°C for 35 min. The labeled cRNA samples were analyzed with the Affymetrix murine genome U74A, -B, and -C array set (Affymetrix, Santa Clara, CA). Hybridization and array scanning were performed according to protocols provided by Affymetrix. Data analysis was performed with Microarray Suite software (Affymetrix).

5′ RACE. 5′ rapid amplification of cDNA ends (RACE) was performed with the 5′ RACE kit (Invitrogen, Carlsbad, CA) according to the manufacturer's protocol. First-strand cDNA was synthesized from cerebellar total RNA with a gene-specific primer (5′-AGAAACCAAAATGAGGCTGCTA-3′) corresponding to the cDNA sequence of expressed sequence tag (EST) clone AI587721. Nested PCR was performed to amplify DNA between the anchor primer and another primer (5′-TGAGGCTGCTAAGAATGGCTTGACTG-3′) specific for AI587721. The product (~1.2 kbp) displayed strong homology to the Trio cDNA sequence (GenBank accession no. NM_007118). A cDNA encoding the Solo/Trio8 open reading frame (ORF) was obtained by RT-PCR with primers 5′-TCTCGAGATGAAAGCTATGGATGTTTTGCC-3′ and 5′-AGAATTCGAATGGAAAGGTAAGGAAACTGAG-3′, derived from the human *Trio* gene (GenBank accession no. NM_007118) and the 1.2-kbp product, respectively. The resulting 5.6-kbp Solo/Trio8 DNA fragment was subcloned into the pGEM-T Easy vector (Promega, Madison, WI) for further sequencing.

In situ hybridization. In situ hybridization was performed as described previously (1). To synthesize cRNA probes for the *Trio* gene, the 357-bp fragment encoding part of the *Solo* gene (nucleotides [nt] 5134 to 5490; DDBJ accession no. AB106872; common probe) and a 339-bp noncoding part of the *Solo* gene (nt 5606 to 5944; *Solo*-specific probe) were subcloned into pBluescript-SKII (+) (Stratagene, La Jolla, CA).

SYBR green-based real-time quantitative RT-PCR. SYBR green-based real-time quantitative RT-PCR was performed with primers 5′-TCTCTCAGACAGACAGCCACGT-3′ (forward) and 5′-TGCTTCATATTAAGGGCAGCAG-3′ (reverse) to amplify Solo/Trio8 cDNA and primers 5′-AGAAGGTGGTGAAGCAGGCAT-3′ (forward) and 5′-ATCGAAGGTGGAAGAGTGGGA-3′ (reverse) for glyceraldehyde-3-phosphate dehydrogenase (GAPDH) cDNA. The quantitative RT-PCR method (user bulletin 2; Applied Biosystems, Foster City, CA) was modified to establish an expression level index for mRNA (1).

Plasmid constructs. With mouse cerebellar cDNA as a template, we performed PCR to construct plasmids encoding full-length (amino acids [aa] 1 to 1849) Solo/Trio8 tagged (N or C terminally) with enhanced green fluorescent protein (EGFP) and FLAG; Solo/Trio8 mutant constructs lacking the C-terminal transmembrane domain [Solo-TM(−) aa 1 to 1830; DDBJ accession no. AB106872] were prepared similarly. The primers used were 5′-CCGCTCGAGATGAAAGCTATGGATGTTTTGCC-3′ [forward primer for N- or C-terminally EGFP-tagged Solo and EGFP-Solo-TM(−)], 5′-GGAATTCGAATGGAAAGGTAAGGAAACTGAGC-3′ (reverse primer for EGFP-Solo), 5′-GGAATTCGCTTGTCATCCTGCGAGTCCGGCTGA-3′ [reverse primer for EGFP-Solo-TM(−)], 5′-CCGCTCGAGCGATGGACTACAAGGACGACGATGACAAGATGAAAGCTATGGATGTTTTGCCA-3′ [forward primer for N-terminally FLAG-tagged Solo and FLAG-Solo-TM(−)], 5′-GGGGGCGGCCGCTCAAATGGAAAGGTAAGGAAACT-3′ (reverse primer for N-terminally FLAG-tagged Solo), 5′-GGGGGCGGCCGCTCACTTGTCATCCTGCGAGTCCG-3′ [reverse primer for N-terminally FLAG-tagged Solo-TM(−)], 5′-CCGCTCGAGATGGATGAAAGCTATGGATGTTTTGC-3′ [forward primer for C-terminally FLAG-tagged Solo and FLAG-Solo-TM(−)], 5′-GGGGGCGGCCGCTTACTTGTCATCGTCGTCCTTGTAGTCAATGGAAAGGTAAGGAAACTGAGC-3′ (reverse primer for C-terminally FLAG-tagged Solo), 5′-GGGGGCGGCCGCTTACTTGTCATCGTCGTCCTTGTAGTCCTTGTCATCCTGCGAGTCCGGCTG-3′ [reverse primer for C-terminally FLAG-tagged Solo-TM(−)]. *Pfu* DNA polymerase was used for PCR, and the amplified products were cloned between the XhoI and EcoRI sites of pEGFP-C3/pEGFP-N1 (Clontech, Palo Alto, CA) or the XhoI and NotI sites of pCI-neo (Promega). To construct the GEF1-inactivated Solo mutant form Solo-AE, the mutations Gln^{1368} to Ala and Leu^{1376} to Glu were introduced into EGFP-Solo with the QuikChange site-directed mutagenesis kit (Stratagene) and primers 5′-CAAACCAGTTGCCCGGATAACAAAGTATCAGCTCGAGTTAAAGGAG-3′ and 5′-CTCCTTTAACTCGAGCTGATACTTTGTTATCCGGGCAACTGGT TTG-3′. All gene constructs were confirmed by DNA sequencing. Expression of the genes for Solo/Trio8 was controlled with a cytomegalovirus promoter.

Cell culture and transient transfections. COS-7, HEK293T, and NIH 3T3 cells were cultured at 37°C in 5% CO_2 in Dulbecco modified Eagle medium containing 10% fetal bovine serum, 100 U/ml penicillin, and 85 μg/ml streptomycin (Invitrogen). Cells were grown on 6- and 24-well or 100-mm dishes and four- and eight-well chamber slides and transfected with equal amounts (0.4 to 3.0 or 20 μg) of plasmid DNA per well with the Lipofectamine 2000 DNA transfection reagent (Invitrogen) according to the manufacturer's instructions and cultured for 8 to 24 h at 37°C.

Rac1 pull-down assay. COS-7 cells were cultured at a density of 2×10^6 cells per 100-mm dish and transfected with 20 μg of an EGFP-Solo expression construct or a control plasmid (pEGFP) as described above. After 16 h, cells were serum starved for 5 h and then washed with phosphate-buffered saline (PBS) and lysed in lysis buffer (25 mM HEPES, [pH 7.5], 150 mM NaCl, 1% [wt/vol] Igepal CA-630, 20 mM $MgCl_2$, 1 mM EDTA, 2% [wt/vol] glycerol, 1 mM Na_3VO_4, 25 mM NaF, complete EDTA-free protease inhibitor mixture [Roche Molecular Biochemicals, Indianapolis, IN]). Cell lysates were centrifuged at 20,000 × *g* for 20 min at 4°C. Rac1 activation was measured with the Rac1 activation assay kit (Upstate Biotechnology Inc., Lake Placid, NY) according to the manufacturer's instructions. Briefly, 0.5 ml of the supernatant (2 mg protein) was added to 10 μl of PAK1–p21–binding domain (PBD)–glutathione *S*-transferase–glutathione agarose beads (Upstate Biotechnology, Inc.), and the mixture was rotated for 1 h at 4°C, followed by three washes of the protein complexes with lysis buffer. PAK1-PBD-bound proteins were dissociated and denatured by boiling in Laemmli sample buffer and subjected to sodium dodecyl sulfate-polyacrylamide gel electrophoresis. The amount of active Rac1 (GTP-bound form) was analyzed by immunoblotting with a monoclonal antibody to Rac1 (Upstate Biotechnology, Inc.).

Cell fractionation. COS-7 cells were transfected with expression plasmids and cultured for 24 h. The cells were homogenized in 300 μl of ice-cold TNE buffer (50 mM Tris-HCl [pH 7.5], 150 mM NaCl, 1 mM EDTA) supplemented with protease inhibitors (Complete Protease Inhibitors; Roche Molecular Biochemicals) and sonicated for 30 s on ice. The homogenates were subjected to centrifugation at 20,000 × *g* for 30 min at 4°C. Supernatants (cytoplasmic fraction) were pooled, and pellets (including light membranes) were washed twice with 0.5 ml of TNE buffer and then lysed for 30 min on ice in radioimmunoprecipitation assay buffer (50 mM Tris-HCl [pH 7.5], 150 mM NaCl, 1 mM EDTA, 0.5%

sodium deoxycholate, 0.1% sodium dodecyl sulfate) with protease inhibitors and subjected to centrifugation at 20,000 × *g* for 30 min at 4°C.

Western blotting. Western blotting was performed as described previously (1). Blots were probed with antibodies to detect EGFP (anti-Living Colors A.v., JL-8; Clontech), anti-FLAG M2 (Sigma, St. Louis, MO), anti-Iκ-B (Cell Signaling Technology, Beverly, MA), anti-platelet-derived growth factor (PDGF) receptor α/β (Upstate Biotechnology, Inc.) or anti-β-actin (Sigma).

Neuronal cultures and transfections. Fetal C57BL/6J mice at embryonic day 16 (E16) were used for the primary culture of embryonic cortical neurons. The brain of each embryo was dissected from the overlying meninges, blood vessels, olfactory bulb, and hippocampus in Hanks' balanced salt solution (HBSS; Gibco, Gaithersburg, MD). Brains were minced with a 0.1-mm blade, and small pieces of the tissues were incubated in 0.25% trypsin–0.04% EDTA (Gibco) for 10 min at 37°C. Digestion was stopped by addition of 2% fetal bovine serum, and the mixture was incubated with 0.01% DNase I (Sigma) at room temperature for 2 min. After being spun down (5 min at 280 × *g*), neuronal cells were resuspended in HBSS. Single-cell suspensions were obtained by trituration and filtered through a 70-μm nylon cell strainer (BD, Bedford, MA) to remove undigested cell aggregates, followed by centrifugation for 5 min at 280 × *g*. Dispersed neurons were plated on Biocoat poly-D-lysine-coated four-well chamber slides (BD) at a density of 2×10^5 or 4×10^5 cells per well in Neurobasal medium (Invitrogen) containing B27 supplement (Invitrogen), penicillin-streptomycin (Invitrogen), and 2 mM L-glutamine (Invitrogen). The cultures were maintained at 37°C in a 5% CO_2 humidified incubator, and half of the medium volume was replaced with fresh medium about every 2 days. Cortical neurons were grown for 6 days in culture and then transfected as described above. For cotransfections, Lipofectamine 2000 reagent (4 μl) and DNA (a total of 1.6 μg of plasmids containing EGFP or EGFP-fused protein and DsRed [pDsRed Express-C1; Clontech] at a ratio of 8:1) were separately suspended in Opti-MEM (50 μl; Invitrogen) and gently combined. After a 20-min incubation at room temperature, the mixture (100 μl) was added to the culture medium (400 μl). DsRed is used to visualize the morphology of the transfected neurons (41). Neurons were allowed to express the transfected protein for 18 h, fixed with 4% formaldehyde in PBS, and immunostained with polyclonal anti-DsRed (1:10,000; rabbit IgG; BD) and mouse monoclonal anti-GFP 3E6 (1:2,000; Molecular Probes, Eugene, OR). Alexa Fluor dye-conjugated secondary antibodies (1:400; Molecular Probes) were used.

Immunofluorescence microscopy. Fluorescence immunostaining was performed as described previously (1). Dilutions of primary antibodies were as follows: anti-EEA1, anti-Bip/GRP78, and anti-GM130 (from BD Biosciences), all 1:100; anti-Rab5a and anti-Rab5b (Santa Cruz Biotech, Santa Cruz, CA), 1:200; anti-Rab7 (Santa Cruz Biotech), 1:100; anti-Tau1 and anti-Map2 (Chemicon International, Temecula, CA), 1:200; anti-calbindin D28k (Swant, Bellinzona, Switzerland), 1:500. All Alexa Fluor dye-conjugated secondary antibodies (Molecular Probes) were diluted 1:200. Immunofluorescence microscopy was performed with an ORCA-ER digital camera (Hamamatsu Photonics, Hamamatsu, Japan), and confocal microscopy was performed with the FLUOVIEW system (Olympus, Tokyo, Japan) or the Leica TCS SP2 spectral confocal scanning system (Leica Microsystems, Wetzlar, Germany) with a 20× objective lens, and images were acquired with Leica Confocal Software version 2.5.

Measurement of EEA1-positive vesicles. For analysis of early endosomes, the number of EEA1-positive vesicles in COS-7 cells expressing EGFP chimeras (and containing an intact nucleus stained with 4′,6′-diamidino-2-phenylindole [DAPI]) was quantified with Image-Pro Plus software version 4.5.1 (Media Cybernetics, Silver Spring, MD). EEA1-positive vesicles (>0.04 μm^2) were assayed by counting 40 cells. After we extracted the morphology of EEA1-positive endosomes with the object-extracting module of Image-Pro Plus, the clustered vesicles were separated with the Watershed Split module in the software. These data were statistically analyzed with Prism software version 3.0c (GraphPad, San Diego, CA). The data were statistically evaluated with one-way analysis of variance, followed by Bonferroni's test.

Endocytosis. Transferrin or Sulforhodamine 101 uptake was assessed as described previously (14, 50). Briefly, COS-7 cells were transfected with EGFP or EGFP-Solo constructs by using Lipofectamine 2000. Seven hours after transfection, the cells were depleted of bovine transferrin by incubation for 45 min in Dulbecco modified Eagle medium containing 0.1% bovine serum albumin and then labeled with human transferrin fluorescently labeled with Alexa-594 (Molecular Probes) at 25 μg/ml or with the fluid-phase fluorescent marker Sulforhodamine 101 (Molecular Probes) at 25 μg/ml for 15 min at 37°C. Internalization was then stopped by placing the cells on ice and washing them three times with ice-cold PBS before formaldehyde fixation. For analysis of endocytosis, fluorescence of Alexa-594-labeled transferrin or Sulforhodamine 101 in COS-7 cells expressing EGFP-Solo chimeras was quantified with Image-Pro Plus software version 4.5.1 with the density histogram module.

Cortical neuron morphometry and analysis. Images of immunostained neurons as described above were captured with an ORCA-ER digital camera, and morphometric analysis of the neurites and their branching was performed with Kurabo Neurocyte Image Analyzer software version 1.5 (KURABO, Osaka, Japan). To analyze the effects on neurite morphology, EGFP-positive cells were assayed by counting at least 60 cells from randomly selected fields. All neurites were measured irrespective of whether they were axons. Neuronal morphology was assessed according to four criteria, pass (number of branches), joint (number of branch points), total length (axon-and-dendrite length), and average maximum neurite length (axon length; Tau1 immunohistochemistry showed that the longest neurite of E16 mouse-derived embryonic cortical neurons was an axon; data not shown). The data were statistically evaluated by one-way analysis of variance, followed by Bonferroni's test.

Organotypic slice culture. The method used for slice culture has been described previously (49). In brief, C57BL/6J mice were decapitated and their brains were dissected and sliced in ice-cold HBSS with a vibratome. P11 cerebella were sliced coronally at a 200-μm thickness. Slices were transferred onto Millicell-CM inserts (Millipore, Bedford, MA) and cultured at the air-medium interface in 5% CO_2 in air at 37°C. Cerebellar slices were cultured essentially as described before (48), in a medium which consisted of 15% heat-inactivated horse serum (Invitrogen), 25% Earle's balanced salt solution (Sigma), 60% Eagle's basal medium (Invitrogen), 5.6 g/liter glucose, 3 mM L-glutamine, 20 nM progesterone, 1 mM sodium pyruvate, 100 U/ml penicillin, 100 μg/ml streptomycin, and Sigma I-1884 supplement (giving final concentrations of 5 μg/ml insulin, 5 μg/ml transferrin, and 5 ng/ml sodium selenite). At 1 day in vitro, cerebellar slices were transfected with small interfering RNA (siRNA).

Transfection of siRNA. We used siRNA to knock down Solo/Trio8 expression in cerebellar-slice cultures. A 21-oligonucleotide siRNA duplex was designed by the siDirect program (RNAi Co., Ltd., Tokyo, Japan). The siRNA oligonucleotide sequences that were used to target the C-terminal transmembrane domain in Solo/Trio8 (region, bp 5483 to 5505) were 5′-GACAAGCAUUACGUUGA UUUG-3′ (sense) and 5′-AAUCAACGUAAUGCUUGUCAU-3′ (antisense) and were synthesized by RNAi Co., Ltd. For the control, scrambled siRNA, silencer negative control no. 1 siRNA (proprietary sequence; Ambion, Austin, TX) was used. To confirm the siRNA effect, the EGFP-Solo plasmid and siRNA targeting Solo/Trio8, as well as a scrambled siRNA control, were cotransfected into COS-7 cells with Lipofectamine 2000 according to the manufacturer's instructions. After 24 h, significant siRNA-mediated suppression of Solo/Trio8 expression was detected by immunocytochemistry with anti-GFP monoclonal antibody 3E6 to estimate the fluorescence intensity of EGFP-expressing cells by fluorescence microscopy. For analysis of the inhibitory efficiency of siRNA, fluorescence signals in COS-7 cells expressing EGFP-Solo were quantified with Image-Pro Plus software version 4.5.1 with the density histogram module. To knock down endogenous Solo/Trio8 expression in Purkinje cells, at 1 day in vitro the siRNA was transfected into cerebellar slices with X-tremeGENE siRNA Transfection Reagent (Roche Applied Science) according to the manufacturer's instructions. In addition, scrambled siRNA no. 1 was transfected as a negative control. After 2 days, the slices were immunostained with anti-calbindin D28k as described below.

Immunohistochemistry. For Purkinje neuron morphometry, Purkinje cells were visualized by immunostaining with a mouse monoclonal antibody against calbindin D28k. The immunostaining method for brain slices has been described previously (48). Briefly, slices were fixed in 4% paraformaldehyde in PBS for 1 h at room temperature and washed three times with PBS. Slices were incubated with 10% normal goat serum in PBS containing 0.3% Triton X-100 for 1 h. Slices were then incubated overnight at 4°C with primary antibody diluted 1:500 in PBS containing 3% normal goat serum and 0.3% Triton X-100 and then washed three times with PBS. Slices were incubated with goat Alexa 488-conjugated secondary antibody diluted 1:200 in PBS containing 1% goat serum and 0.3% Triton X-100 for 1 h at room temperature and washed three times with PBS. Images of immunostained Purkinje neurons were captured with the Leica TCS SP2 spectral confocal scanning system (20× objective lens), and morphometric analysis of the axons was performed with the Kurabo Neurocyte Image Analyzer as described above.

Nucleotide sequence accession number. The nucleotide sequence of mouse Solo/Trio8 has been deposited in the DDBJ nucleotide sequence database under accession number AB106872.

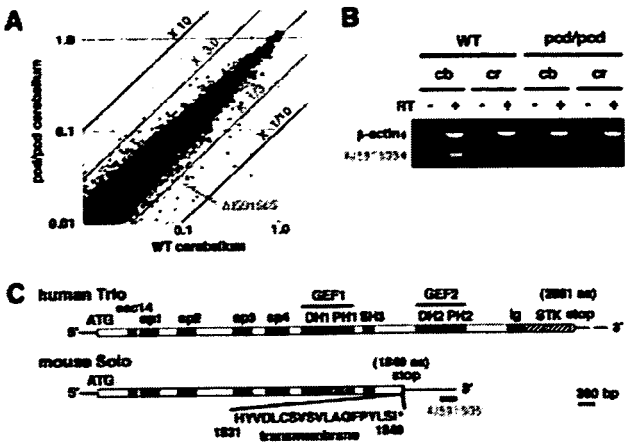

FIG. 1. Identification of a cDNA sequence predominantly expressed in Purkinje neurons. (A) Scattergram analysis of microarray data. Cerebellar cDNAs derived from pcd and WT mice were analyzed with DNA microarrays, and the average signal from each gene was normalized to the GAPDH signal and plotted to yield the scattergram. The AI591505 cDNA is indicated on the plot. (B) RT-PCR analysis of AI591505 transcript expression in the cerebella (*cb*) and cerebra (*cr*) of pcd and WT mice, respectively. PCRs for the β-actin gene (internal control) and AI591505 were performed in a single tube. (C) Structural relationship between the gene for Solo/Trio8 and a consensus of human Trio genes. Protein domains are indicated within the bars, and the 5′ and 3′ noncoding regions are indicated by horizontal lines. The domains shown are as follows: sec14, sec14p-like putative lipid binding domain; sp, spectrin-like domain; DH, Dbl homology domain; PH, pleckstrin homology domain; SH3, Src homology 3 domain; Ig, Ig-like domain; STK, serine/threonine kinase domain.

RESULTS

DNA microarray analysis of the pcd mouse cerebellum. Since no exhaustive gene expression analysis of the pcd mouse has been reported to date, we evaluated changes in cerebellar gene expression from P24 pcd mice (with 70 to 80% Purkinje neuronal loss) and WT mice with DNA microarrays containing almost 6,000 characterized genes and 30,000 ESTs. A comparison between two pcd mice and two WT mice revealed pcd-specific variability in gene expression (Fig. 1A). A scattergram constructed from hybridization data of 12,518 highly expressed genes (those having signals >0.01% of that measured for GAPDH) revealed only six upregulated genes (>3-fold) and 26 downregulated genes (<0.33-fold) in pcd mice (Table 1).

EST AI591505 is expressed exclusively in Purkinje neurons. Among the downregulated genes, we identified uncharacterized EST clone AI591505 (GenBank) (Fig. 1A; Table 1). AI591505 is 236 bp in length and has no homology with any annotated genes. The as-yet-uncharacterized AI591505 transcript was highly expressed in the normal mouse cerebellum (~10% of the GAPDH signal in the WT array; Fig. 1A). AI591505 was of interest because its decreased expression level in the pcd cerebellum suggested that it is a relatively highly expressed uncharacterized Purkinje neuron-specific gene. The decreased expression of the AI591505 transcript in the pcd cerebellum was confirmed by RT-PCR analysis with the cerebra and cerebella of pcd and WT mice, respectively. This transcript was expressed predominantly in the cerebellum, and expression in the pcd mouse was clearly lower than in the WT mouse (Fig. 1B). In situ hybridization showed that the transcript was expressed predominantly in the WT Purkinje cell layer at P24 (Fig. 2B) but not in the E16 brain (Fig. 2A) and was decreased in pcd Purkinje cells (Fig. 2B, c to i). Relatively low-level expression was also detected in the olfactory bulb and hippocampus (Fig. 2B, c to e). The expression level of the AI591505 gene in the P7 pcd cerebellum (before onset of degenerative loss of Purkinje neurons) was equivalent to that in the P7 WT cerebellum (data not shown), although the *Nna1* (pcd causative gene) expression level was significantly decreased in the P7 pcd cerebellum (data not shown), suggesting that the AI591505 gene is not a downstream gene directly controlled by *Nna1* expression.

Identification of Solo/Trio8, a Trio splice variant, expressed predominantly in Purkinje neurons. An additional search of databases identified another EST, AI587721, containing a region overlapping the AI591505 sequence. 5′ RACE with the AI587721 sequence yielded a 1.2-kbp cDNA clone from the cerebellum. A search of GenBank revealed that this clone contained a part of the *Trio* sequence (accession no. NM_007118). To clone the entire ORF, a PCR was performed with primers for *Trio* (forward) and the cDNA clone (reverse)

TABLE 1. Genes with altered expression in the pcd cerebellum

Gene (accession no.)	Relative expression		pcd/WT ratio
	WT[a]	pcd[a]	
Genes upregulated in pcd cerebellum			
CPP32 (U63720)	0.042	0.137	3.29
TYRO (AF024637)	0.027	0.088	3.25
Slp-w7 (X06454)	0.024	0.082	3.45
UN[b] (AK084804)	0.015	0.046	3.08
UN[b] (BC055829)	0.014	0.043	3.00
DnaJ-like (AK053156)	0.011	0.036	3.37
Genes downregulated in pcd cerebellum			
IP3R1 (X15373)	0.533	0.054	0.10
28-kDa calbindin (D26352)	0.525	0.032	0.06
NK6 (AK083449)	0.396	0.113	0.29
PCP-1 (M21530)	0.356	0.040	0.11
RGS8 (AK044337)	0.322	0.084	0.26
GluR1 (BC056397)	0.299	0.098	0.33
PCP-2 (M21532)	0.298	0.056	0.19
DRR1-like (AK032875)	0.162	0.040	0.24
Ca^{2+}-ATPase (BC026147)	0.146	0.019	0.13
PKC-γ (L28035)	0.135	0.024	0.18
EAAC4 (D83262)	0.131	0.017	0.13
MGF (M57647)	0.129	0.031	0.24
Delphilin (AF099933)	0.127	0.013	0.10
rp S18a (AB049953)	0.114	0.031	0.27
AI591505	0.094	0.028	0.30
Tubulin ligase (AB093278)	0.087	0.014	0.16
Metalloprotease (AK034528)	0.074	0.023	0.31
Shank2 (AB099695)	0.066	0.019	0.28
PH protein (AK028383)	0.060	0.013	0.22
NSC dendrite regulator (BC030853)	0.056	0.017	0.31
Aspartate-β-hydroxylase (AF289488)	0.056	0.017	0.31
Ca^{2+} channel α1G (AJ012569)	0.055	0.011	0.20
Tm4sf10 (BC019751)	0.049	0.015	0.31
Chemokine (AY241872)	0.039	0.013	0.32
Oxytocin-neurophysin I (M88355)	0.038	0.011	0.28
ARM repeat protein (AK044219)	0.033	0.010	0.30

[a] Expression level relative to GAPDH (average from two WT or pcd mice).
[b] UN; uncharacterized gene.

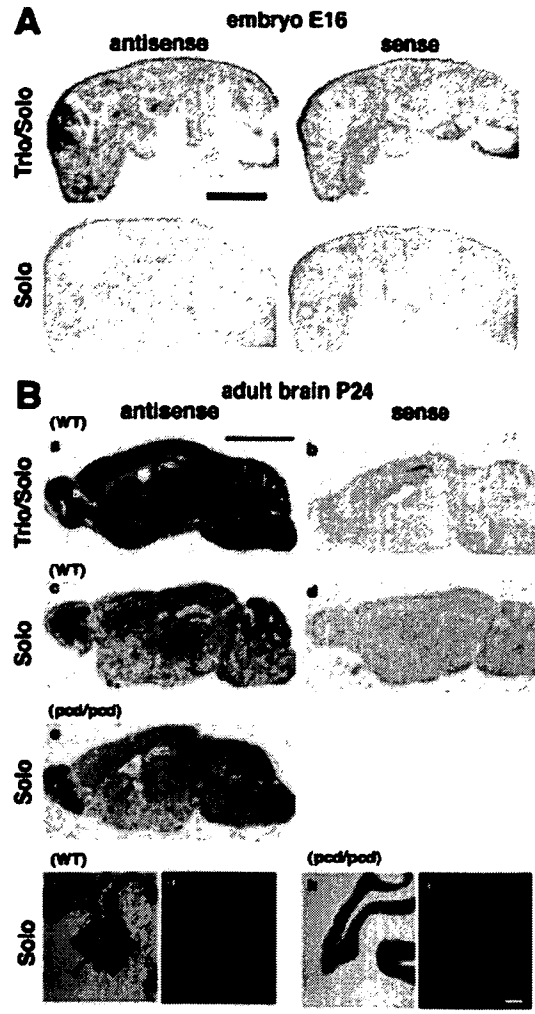

FIG. 2. Expression of Solo and Trio mRNAs in the mouse embryo and adult mouse brain. (A) In situ hybridization analysis of the mouse embryo (E16) with Solo-specific and Solo/Trio-common cRNA probes. Antisense and sense probes were prepared with Solo-specific and Solo/Trio (common to both) regions of the cDNA, respectively, and hybridized with tissue sections from an E16 mouse whole embryo. Bar = 5 mm. (B) In situ hybridization analysis of Solo transcript (AI591505) in P24 WT (a to d, f, g) and pcd (e, h, i) brains. Antisense and sense probes were prepared from Solo-specific and Solo/Trio (common to both) regions of the cDNA, respectively, and hybridized with tissue sections from P24 mouse whole brains. Regions in part a are labeled as follows: cb, cerebellum; ctx, cortex; hp, hippocampus; ob, olfactory bulb. The arrow in part f indicates the Purkinje cell layer, and the bars in part f indicate the molecular (lower) and granule (upper) layers. Bar in part a = 5 mm (same scale for parts a to e). Bar in part i = 200 μm (same scale for parts f to i).

to yield a cDNA with an entire ORF of 5,550 bp encoding 1,849 aa (Fig. 1C) from the cerebellum. The human *Trio* ORF contains 8,586 bp encoding 2,861 aa (6) (Fig. 1C); the cloned cDNA lacked the region between nucleotides 5491 and 8586 but contained a distinct 874-bp sequence at the 3′ end (Fig. 1C). A search of GenBank revealed the corresponding exon in the mouse *Trio* gene (data not shown), suggesting that the transcript is an alternatively spliced product of the *Trio* gene. We thus named this isoform Solo, for *s*hort-form *s*plice variant of Trio. Solo contains an N-terminal sec14-like domain, spectrin-like repeats, a GEF1 domain, one SH3-like domain, and the unique C-terminal hydrophobic sequence HYVDLCSVS VLAQFPYLSI (aa 1831 to 1849, Fig. 1C). Computational analyses with a protein motif search program (http://motif.genome.ad.jp/) suggested that this C-terminal hydrophobic sequence resembles transmembrane helices of G-protein-coupled receptors (data not shown). McPherson et al. recently reported identification of rat Trio variants (25). Among them, the amino acid sequence of rat Trio8 was highly similar (99.7%) to that of mouse Solo, suggesting that Solo is a mouse homologue of Trio8.

To delineate the expression patterns of the genes for Solo/Trio8 and Trio in the mouse brain, we performed in situ hybridization with Solo-specific and Solo/Trio-common cRNA probes. The Solo/Trio-common probe signal was distributed over the entire mouse brain, and more-intense signals were observed in the hippocampus, olfactory bulb, cortical layers, and cerebellum (Fig. 2B, a and b). This hybridization pattern differed from that of the Solo-specific probe, which was predominantly expressed in the Purkinje cell layer of the cerebellum (Fig. 2B, c, d, f, and g). To determine if Solo/Trio8 mRNA is actually translated into protein, we performed Western blot analysis with a polyclonal antibody recognizing a 14-aa internal sequence near the N terminus of Solo and Trio (anti-Solo/Trio antibody). The immunoblot showed a 210-kDa immunoreactive band in the mouse cerebellum, in good agreement with the expected molecular mass of Solo (212 kDa) (data not shown). McPherson et al. (25) also detected a 210-kDa rat Trio8 protein in the rat cerebellum by Western blotting with an antibody against Trio8. The size of the Solo/Trio8 protein in mouse and rat cerebella was identical to that measured in COS-7 cells transfected with the Solo expression vector (Fig. 3C). Our antibody against Solo/Trio did not work well in immunohistochemical, immunocytochemical, and fractionation experiments (data not shown), so we were unable to determine the protein expression pattern in the brain.

Guanine nucleotide exchange activity of Solo/Trio8 for a Rho family GTPase. The GEF1 domain of Trio activates RhoG and Rac1, whereas GEF2 acts on RhoA (3). We addressed whether the GEF1 domain of Solo/Trio8 has guanine nucleotide exchange activity for Rac1 by a pull-down assay with the PBD of PAK1, which specifically binds to GTP-bound Rac1 (active form) but not to the inactive GDP-bound form (4). The amount of activated Rac1 in COS-7 cells transfected with the EGFP-Solo construct was markedly increased compared with that in negative control cells transfected with EGFP (Fig. 3B, top). Previous studies demonstrated that a double amino acid mutant form of Trio (Q1368A and L1376E within the GEF1 domain) completely abolishes the GEF1 activity (10, 23). The Q1368A and L1376E double mutation (EGFP–Solo-AE, Fig. 3A) abolished EGFP-Solo-mediated Rac1 activation in COS-7 cells (Fig. 3B, top). The C-terminal hydrophobic sequence (HYVDLCSVSVLAQFPYLSI; Fig. 1C) of Solo/Trio8 was predicted by a protein motif search program to function as a membrane-anchoring domain (data not shown). Deletion of this putative domain (EGFP–Solo-TM(−), Fig. 3A) did not affect Rac1 activation (Fig. 3B, top). There was no significant difference in the total amount of Rac1 expressed in COS-7 cells transfected with the EGFP, EGFP-Solo, EGFP–